Along-Strike Variations of Alaska Subduction Zone Structure and Hydration Determined From Amphibious Seismic Data

Zongshan Li[1], Douglas A. Wiens[1], Weisen Shen[2], Donna J. Shillington[3]

[1]Department of Earth, Environmental, and Planetary Sciences, Washington University, St. Louis, MO, 63130, USA.

[2]Department of Geosciences, Stony Brook University, Stony Brook, NY, 11794, USA.

[3]Northern Arizona University, School of Earth and Sustainability, Flagstaff, AZ 86001, USA.

Corresponding author: Zongshan Li (zongshan.li@wustl.edu)

Key Points:

- Crustal thickness of the inner forearc (35-42 km) generally exceeds that of the volcanic arc, but becomes variable in the Shumagin segment.

- The Shumagin segment has more incoming plate mantle hydration than the Semidi segment, aligning with abundant plate bending normal faults.

- Hydration extends to depths of 18 km below the Moho, indicating more water subducts than most previous estimates.

20 **Abstract**

21 We develop a 3-D isotropic shear velocity model for the Alaska subduction zone using data from
22 seafloor and land-based seismographs to investigate along-strike variations in structure. By
23 applying ambient noise and teleseismic Helmholtz tomography, we derive Rayleigh wave group
24 and phase velocity dispersion maps, then invert them for shear velocity structure using a
25 Bayesian Monte Carlo algorithm. For land-based stations, we perform a joint inversion of
26 receiver functions and dispersion curves. The forearc crust is relatively thick (35-42 km) and has
27 reduced lower crustal velocities beneath the Kodiak and Semidi segments, which may promote
28 higher seismic coupling. Bristol Bay Basin crust is relatively thin and has a high-velocity lower
29 layer, suggesting a dense mafic lower crust emplaced by the rifting processes. The incoming
30 plate shows low uppermost mantle velocities, indicating serpentinization. This hydration is more
31 pronounced in the Shumagin segment, with greater velocity reduction extending to 18 ± 3 km
32 depth, compared to the Semidi segment, showing smaller reductions extending to 12 ± 3 km
33 depth. Our estimates of percent serpentinization from V_S reduction and V_P/V_S are larger than
34 those determined using V_P reduction in prior studies, likely due to water in cracks affecting V_S
35 more than V_P. Revised estimates of serpentinization show that more water subducts than
36 previous studies, and that twice as much mantle water is subducted in the Shumagin segment
37 compared to the Semidi segment. Together with estimates from other subduction zones, the
38 results indicate a wide variation in subducted mantle water between different subduction
39 segments.

40

41 **Plain Language Summary**

42 This study uses seismic data from the 2018-2019 Alaska Amphibious Community Seismic
43 Experiment and other land stations to image the 3-D seismic velocity structure of the Alaska
44 subduction zone. The analysis combines constraints from both Rayleigh waves and converted
45 body waves. The results provide insight into the distinct lateral variations observed for many
46 properties of the subduction zone. Thick, low-velocity forearc crust is found beneath the Kodiak
47 and Semidi segments, which may be related to the higher seismic coupling in these regions. The
48 Bristol Bay Basin has thin crust with a high velocity lower layer, suggesting a dense mafic lower
49 crust emplaced by the extensional processes that formed the basin. Low velocities in the
50 incoming plate near the trench in the Shumagin segment indicate pronounced mantle hydration,
51 extending to about 18 km below the Moho. Together with estimates from other subduction
52 zones, the results indicate a wide variation in subducted mantle water between different
53 subduction segments.

54

55 **1 Introduction**

56   Subduction zones are the locus of many of the most important geological processes,
57 including earthquakes, volcanism, sediment accretion, and the formation of new crust. It is
58 particularly useful to study the along-strike variability of these parameters within a single large
59 subduction segment. The Alaska subduction zone is one of the most tectonically active plate
60 boundaries worldwide, with numerous large earthquakes and active volcanoes. In the Alaska
61 Peninsula region, the subducting plate has an intermediate age (~50-55 Ma) and a relatively
62 uniform convergence rate (~63 mm/yr) (DeMets et al., 2010), but the seismicity, geodetic

63 locking, and earthquake rupture zones show distinct along-strike variations (e.g., Davies et al.,
64 1981; Shillington et al., 2015; Xiao et al., 2021) (Figure 1). These along-strike variations make
65 it an ideal place to study many subduction zone processes, including earthquake and geodetic
66 properties, forearc and backarc tectonics, and the pathways of water through the subduction
67 system. Many aspects of the along strike-variations in these processes can be revealed by
68 detailed imaging of variations in subduction zone structure.

69 Subduction zones are also the key to understanding the long-term water cycle on Earth,
70 since subducting oceanic plate serves as the only mechanism to carry water into the deep interior
71 of the Earth. The water flux from hydrated oceanic plates is essential for arc volcanism and may
72 control along-arc changes in magma chemistry (Sadofsky et al., 2008; Manea et al., 2014).
73 Furthermore, water greatly lowers the viscosity of the surrounding mantle, which may be highly
74 important for the dynamics of subduction (e.g., Hebert et al., 2009). Hydration of downgoing
75 slabs is likely to be ubiquitous in the worldwide oceanic trench regions, but the extent of mantle
76 hydration is poorly constrained, and remains the main uncertainty in the global water cycle (van
77 Keken et al., 2011). A previous study of the Alaska subduction zone suggested strong along-
78 strike variations in mantle hydration of the incoming plate in the offshore Alaska Peninsula
79 region (Shillington et al, 2015).

80 Active-source studies have revealed low mantle velocities in the plate bending regions of
81 many subduction zones that are interpreted as indicating serpentinization of mantle peridotite
82 (Ranero et al., 2003; Van Avendonk et al., 2011; Shillington et al., 2015; Fujie et al., 2018;
83 Arnulf et al., 2022), including offshore of the Shumagin segment (Shillington et al., 2015;
84 Acquisto et al., 2022b; Shillington et al., 2022). However, in most cases active-source studies
85 provide only limited constraints on the depth extent of mantle serpentinization, leaving large
86 uncertainties in the amount of bound water subducted. Passive-source studies, on the other hand,
87 are able to image the deeper structure of the incoming plate and place constraints on the depth of
88 serpentinization. A passive source study in the Mariana subduction zone found that the mantle
89 hydration at the Mariana trench extends to ~24 km below the Moho (Cai et al., 2018), suggesting
90 the total amount of water input into the Mariana trench is at least 4.3 times more than previous
91 estimates (van Keken et al., 2011). Since the Alaska Subduction Zone differs from Mariana in
92 terms of incoming plate age (~50 Ma, as opposed to ~150 Ma for Mariana), and shows extensive
93 along-strike variation in incoming plate fabric and faulting, it represent an excellent target to test
94 the possible widespread occurrence of deeper incoming plate hydration.

95 The 2018-2019 Alaska Amphibious Community Seismic Experiment (AACSE) deployed
96 an amphibious array of 75 ocean bottom seismographs (OBS) and 30 land seismographs,
97 complemented by a temporary nodal array on Kodiak Island and an active-source seismic
98 experiment offshore the Semidi segment and Kodiak Island (Barcheck et al., 2020). The
99 amphibious array of AACSE, along with several other simultaneously operating land seismic
100 networks, provide a unique opportunity to image subduction zone structure. In this study, we use
101 this dataset to image the along-strike variations in the Alaska subduction zone structure and
102 provide important constraints on the hydration of the downgoing plate, as well as the structure
103 and tectonics of the forearc and backarc regions. In contrast to previous surface wave
104 tomographic studies that carry out large-scale imaging of the entire Alaska region, or analyze
105 only one type of seismic data, our analysis includes both ambient noise tomography and
106 teleseismic earthquake Helmholtz tomography, as well as P-wave receiver functions, to better
107 constrain the Alaska subduction zone with higher resolution.

108

2 Tectonic Setting and Previous Work

110   From west to east, the plate boundary can be divided into three main segments, named
111 Shumagin, Semidi, and Kodiak segments after the corresponding forearc islands (Figure 1b). The
112 Shumagin segment, also called Shumagin Gap, is a region with abundant interplate and
113 intermediate-depth earthquakes (Figure 1a), but has not ruptured during a great earthquake (M ≥
114 8) for at least 150 years (Davies et al., 1981). The Semidi and Kodiak segments, however, have
115 much less seismicity at all depths and have ruptured in several historical great earthquakes (e.g.,
116 1938 M8.2; 1946 M8.6; 1964 M9.2) (Davies et al., 1981) (Figure 1b). In recent years, two
117 megathrust events (July 22, 2020 M7.8 Simeonof earthquake and July 29, 2021 M8.2 Chignik
118 earthquake) occurred in the Semidi segment (Figure 1b). The slip model of the 2021 M8.2
119 Chignik earthquake suggests that its rupture zone is within the estimated 1938 M8.2 aftershock
120 zone (Chengli Liu et al., 2022; He et al., 2023). The 2020 M7.8 Simeonof earthquake, however,
121 expanded westward and is considered to have ruptured the eastern Shumagin Gap and a little bit
122 of the westernmost Semidi segment (Liu et al., 2020), and was followed by an unusual strike-slip
123 M7.6 event within the Shumagin Gap on October 19, 2020 (Y. Jiang et al., 2022). In addition,
124 geodetic results suggest that the plate motion along the megathrust changes from creeping nearly
125 aseismically in the western portion of the Shumagin segment, to weakly coupled in the eastern
126 portion of Shumagin segment, to intermediate coupled in the Semidi segment, to strongly locked
127 in the Kodiak segment (S. Li & Freymueller, 2018; Drooff & Freymueller, 2021; Xiao et al.,
128 2021). The characteristics of double seismic zones (DSZs) also show clear variations between
129 each segment (Wei et al., 2021; Aziz Zanjani & Lin, 2022).

130   The distribution of incoming plate fabric, sediment thickness, and plate bending faults are
131 also highly variable along strike. The incoming plate fabric has a variable orientation resulting
132 from the spreading along the Kula plate and Kula-Farallon ridge (e.g., Lonsdale, 1988; Bradley
133 et al., 2003). Magnetic anomalies on the incoming Pacific plate show that the paleo-spreading
134 direction changes from sub-parallel to the trench axis in the Shumagin segment to sub-
135 perpendicular to the trench axis in the Semidi and Kodiak segments (Figure 1a). As for the
136 sediment thickness of the incoming plate, Shumagin segment has disrupted sediments (~0.5 km)
137 while Semidi segment has relatively thick and stable sediment (~1 km) (Shillington et al., 2015;
138 J. Li et al., 2018). Furthermore, the Shumagin segment shows abundant outer-rise faults whereas
139 the Semidi and Kodiak segments have few outer-rise faults (Shillington et al., 2015).

140   A previous active source study compared profiles between Shumagin and Semidi
141 segments, finding much stronger velocity reduction and thus hydration in the Shumagin segment
142 (Shillington et al., 2015; Shillington et al., 2022). They suggest that hydration is controlled by
143 the intensity of plate-bending faults, which is in turn strongly influenced by the plate abyssal hill
144 fabric formed during spreading (e.g., D. H. Christensen & Ruff, 1988; Masson, 1991; Ranero et
145 al., 2003). Small faults from the plate spreading fabric are parallel to magnetic anomalies, being
146 oriented roughly trench-parallel in the Shumagin segment but at high angles to the trench axis in
147 the Semidi segment (Figure 1; Figure 8a). However, other studies suggest that factors like the
148 trench-ridge angle (Fujie et al., 2018), or slab curvature (Naliboff et al., 2013) may be more
149 important in controlling the along-strike variation.

150   The overriding plate in the Alaska Peninsula is built from a series of accreted terranes,
151 including the Peninsula Terrance, the Chugach Terrane, and the younger Prince William Terrane

152   (Bruns et al., 1985; Horowitz et al., 1989). Active-source projects EDGE (Moore et al., 1991)
153   and ALEUT (Shillington et al., 2015; Bécel et al., 2017) have revealed variations in P-wave
154   velocity and upper plate structures associated with these accreted terranes. The crustal structure
155   of the Kodiak Shelf shows a series of arched reflectors in the lower crust that coincide with low-
156   velocity rocks, providing evidence for large-scale underplating between Kenai Peninsula and
157   Kodiak Island (Moore et al., 1991; Ye et al., 1997). The forearc structure is spatially complex as
158   a result of this accretion history, and may provide important controls on the seismogenic
159   characteristics of megathrust earthquakes, such as their down-dip limit and the seismogenic
160   extent (Kuehn, 2019; Shillington et al., 2022). In Shumagin segment, the outer forearc has a
161   small frontal prism and hosts active crustal-scale splay faults, indicating a typical tsunamigenic
162   structure (Bécel et al., 2017; von Huene et al., 2021). Downdip variations in the seismic
163   reflection character of the plate interface at the eastern Shumagin segment have been linked to
164   the changes in fault structure and corresponding seismogenic behaviors (J. Li et al., 2015).
165   Along-strike variations in pore-fluid pressure and sediment thickness appear to correlate with
166   changes in seismicity, locking, and earthquake history (J. Li et al., 2018).

167   The volcanic arc and backarc also show variations between each segment. Active
168   volcanoes are widely distributed along the Alaska Peninsula and the southwestern Alaska Range
169   (Figure 1b). Alaska has about 100 volcanoes active in the past 11,000 years and more than 50
170   volcanoes considered historically active since 1760 (Cameron et al., 2018). In spatial
171   distribution, both Semidi and Kodiak segments have strong arc volcanism, especially at the arc
172   front of the Kodiak segment. The composition of arc lavas varies along the Alaska Peninsula,
173   which has been attributed to variations in water and sediments entering the subduction zone (Wei
174   et al, 2021). The Bristol Bay Basin, located on the north side of the Alaska Peninsula in the
175   backarc of the Shumagin and Semidi segments, contains a significant thickness of sediments.
176   Active-source studies and numerical models suggest that Bristol Bay formed mainly through two
177   stages. In early or middle Eocene through late Miocene phase, extension led to fault-controlled
178   subsidence. Then a late Eocene through Holocene phase of volcanic-arc loading or northward
179   prograding delta lead to flexural subsidence (Walker et al., 2003).

180   Previous passive source seismic studies have mostly investigated the structure of
181   continental portions of southern and central Alaska (Eberhart-Phillips et al., 2006; Qi et al.,
182   2007; Y. Wang & Tape, 2014; Ward, 2015; Martin-Short et al., 2018; Yang & Gao, 2020) or
183   along the Alaska Peninsula (You Tian & Zhao, 2012; Janiszewski et al., 2013). Benefiting from
184   the Earthscope Transportable Array that deployed in Alaska from 2014 until 2021, the entire
185   Alaska region has also been imaged for both isotropic and anisotropic velocity structures (C.
186   Jiang et al., 2018; Ward & Lin, 2018; Feng & Ritzwoller, 2019; Gou et al., 2019; Berg et al.,
187   2020; Feng et al., 2020) as well as seismic velocity interfaces (Gama et al., 2022). However, the
188   lack of seismic array coverage offshore the Alaska Peninsula and the large-scale
189   parameterization of the studies leads to the lack of resolution in the incoming plate and forearc
190   area of the Alaska subduction zone.

191   Several recent studies have taken advantage of the 2018-2019 AACSE dataset to carry
192   out more detailed studies of the Alaska Peninsula region. A nodal seismograph array installed on
193   Kodiak Island was used to image the structure immediately beneath Kodiak island (Onyango et
194   al, 2022). Airgun shots recorded by AACSE ocean bottom seismographs provide improved
195   estimates of shallow crustal structure in the offshore peninsula area (Acquisto et al., 2022a).
196   Body wave tomography (Gou et al., 2022; F. Wang et al., submitted), and surface wave

197 tomography (Feng, 2021; Chuanming Liu et al., 2022) provide improved images of the structure
198 beneath the region. Constraints on azimuthal anisotropy are provided by a recent shear-wave
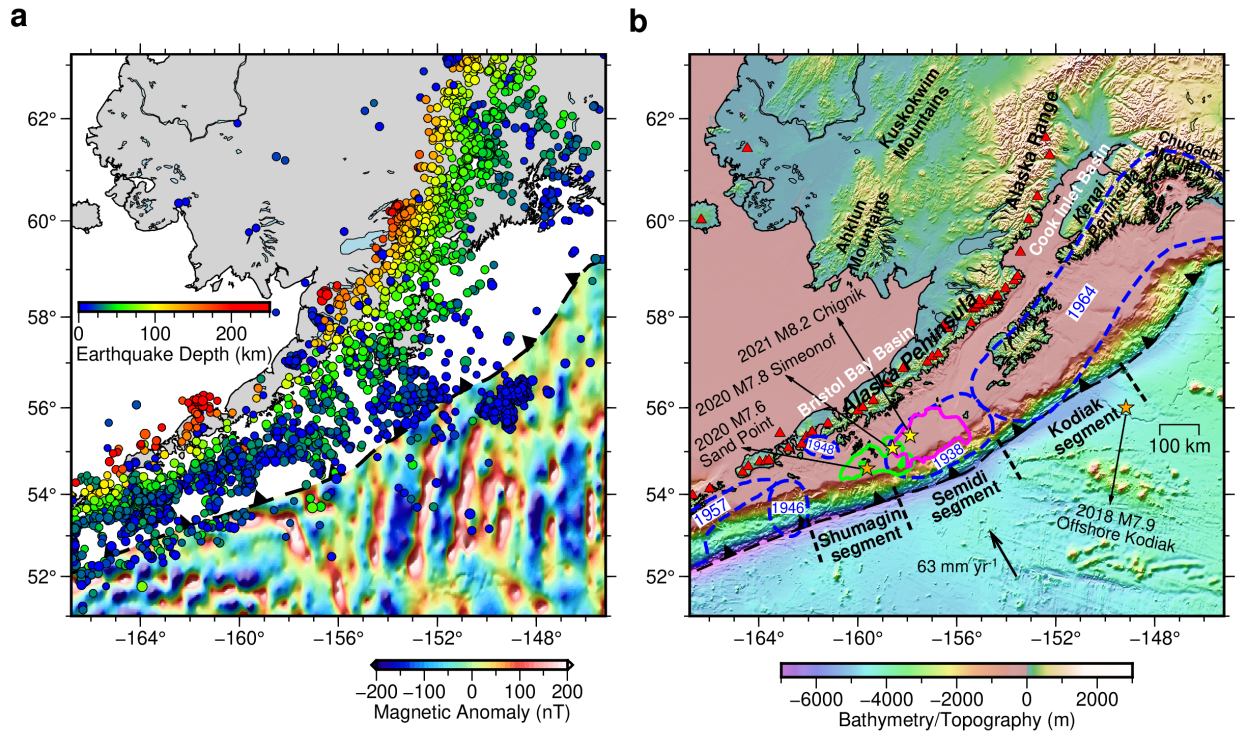199 splitting study (Lynner, 2021).

200

201

202 **Figure 1**. The geological setting of the Alaska subduction zone, with the plate boundary marked
203 as the dashed black line with triangles. **(a)** The magnetic anomaly of the incoming Pacific plate
204 and earthquake distribution. The incoming plate magnetic anomalies are from EMAG2v3 (Meyer
205 et al., 2017). The earthquakes with M ≥ 4 from the Alaska Earthquake Information Center
206 (AEIC) catalog from 1990 to 2022 and from the AACSE catalog during the AACSE deployment
207 (Ruppert et al., 2022) are plotted as circles colored by their epicentral depths. **(b)** Great
208 earthquake rupture zones and prominent geological regions. Dashed blue contours show the
209 rupture zones of historical earthquakes (Davies et al., 1981). Yellow stars indicate the epicenters
210 of megathrust events: the 2020 M7.8 Simeonof earthquake and 2021 M8.2 Chignik earthquake,
211 and their rupture zones are shown as green and magenta, respectively (Liu et al., 2020; Chengli
212 Liu et al., 2022). Orange stars show the epicenters of the 2018 M7.9 Offshore Kodiak earthquake
213 and the 2020 M7.6 Sand Point earthquake, both of which are intraplate strike-slip events. The
214 convergence rate between the Pacific plate and the North American plate is relatively uniform in
215 the study area, thus a black arrow with the average value (~63 mm yr^{-1}) is marked on the
216 incoming plate (DeMets et al., 2010).

217

218 **3 Data and Method**

219 3.1 Seismic data

220   Data for this analysis come from the Alaska Amphibious Community Seismic
221 Experiment (AACSE; May 2018 – September 2019) as well as several land seismograph
222 networks. The AASCE deployed an array of broadband seismic stations covering the Alaska-
223 Aleutian Trench and the Alaska Peninsula from May 2018 to September 2019, including 75
224 ocean bottom seismographs (OBSs) and 30 land stations (Barcheck et al., 2020). At the same
225 time, the EarthScope Transportable Array (TA) was operating many seismic stations throughout
226 Alaska. Therefore, land stations from TA and several other networks also augment the
227 amphibious seismic array.

228   After excluding those stations with non-broadband sensors, or poor quality, this study
229 includes 61 AACSE ocean bottom seismographs (OBSs), 30 AACSE land stations, and 179 land
230 stations of other networks (network codes: AT, AK, II, AT, GM, YG, AV) to analyze the
231 Rayleigh wave dispersion. Altogether, we use a dense amphibious array of 270 seismic stations
232 to perform tomographic inversion (see Section 2.3 to 2.5). In addition, we use 40 land stations
233 that operated outside the AACSE deployment time period for P-wave receiver functions only
234 (see Section 2.6). The detailed distribution of stations that contribute to this study is shown in
235 Figure 2.

236   Some AACSE land sites on Kodiak Island and the Alaska Peninsula experienced bear
237 attacks on their GPS antennae and lost time synchronization. Some OBSs have possible clock
238 drift due to the early shutdown of their dataloggers and clocks. We test and correct the time drift

239   using a cross-correlation technique (Stehly et al., 2007; Gouédard et al., 2014); please see the
240   supplement of Barcheck et al. (2020) for the details on the method and correction results.
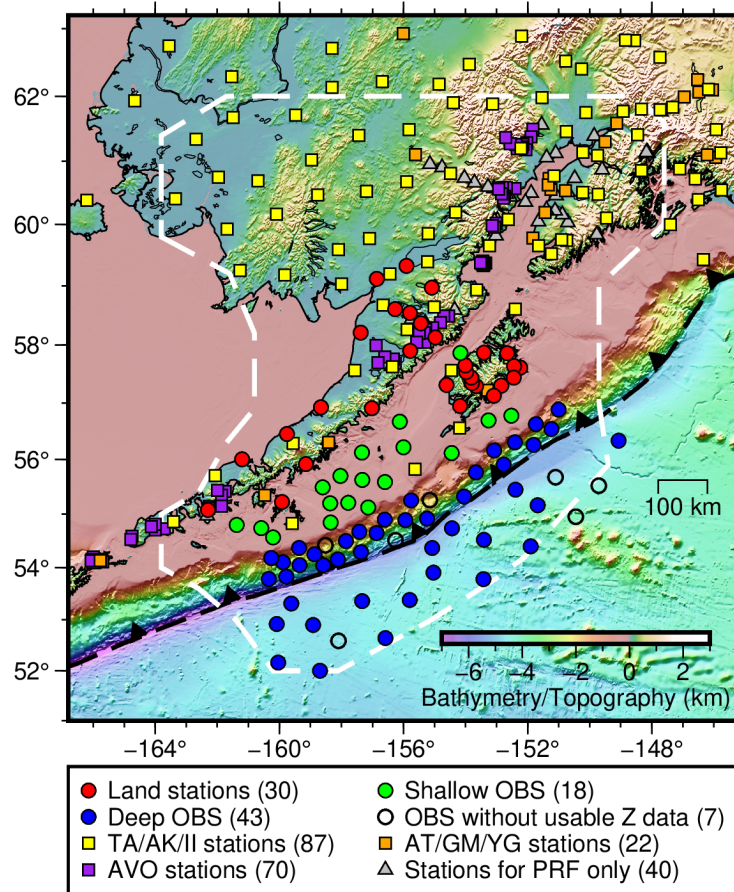
241

242

243   **Figure 2**. A map of the seismic stations used in this study. The stations are plotted with different
244   shapes and colors according to their networks and types. Red, green, and blue circles represent
245   land stations, shallow ocean bottom seismographs (OBS), and deep OBS, respectively, that were
246   deployed by the AACSE project (Barcheck et al., 2020), OBSs without usable vertical
247   component data are shown as blank circles. Yellow squares are the land stations of the
248   Transportable Array (TA), Alaska Network (AK), and Global Seismic Network. Orange squares
249   are the land stations of the Tsunami Warning, and U.S. Geological Survey Networks (GM).
250   Purple squares are the stations belonging to Alaska Volcano Observatory (AVO) network, which
251   are clustered around volcanoes. Gray triangles are those stations that are used for receiver
252   function analysis only. Note that the 4 OBSs that were not recovered and 3 OBSs that failed to

253   record any seismic or pressure data are not included here (Barcheck et al., 2020). White lines
254   encloses the study area defined in Section 2.5.

255   3.2 Pre-processing the OBS data

256   OBS data usually contain noises that are not present in land seismic records, since the
257   seafloor environment generally has higher noise levels in the long-period seismic band. Previous
258   work has shown that for OBS vertical component data, there are two main noise sources: one is
259   tilt noise resulting from variable ocean-bottom currents tilting the instrument and causing
260   horizontal noise to be recorded by the vertical component; the other is compliance noise resulting
261   from the vertical movements of seafloor due to sea bottom pressure changes resulting from
262   infragravity waves (Webb & Crawford, 1999; Crawford & Webb, 2000). The similarity of tilt
263   noise on vertical and horizontal components, and the similarity of compliance noise on the
264   vertical component and the differential pressure gauge (DPG) suggest that both noises on the
265   vertical component can be largely removed by estimating spectral transfer functions (Bell et al.,
266   2014). For various types of AACSE OBSs, there are three different types of pressure channels:
267   differential pressure gauge (DPG), absolute pressure gauge (APG), and hydrophone. Through
268   tests and comparisons, we found that both DPG and APG are able to remove the compliance
269   noise, while the hydrophone is not very successful.

270   The spectral transfer functions used for noise removal are best calculated from time series
271   without earthquakes, so we estimate transfer functions by combining methods described in
272   Janiszewski et al. (2019) and Ma et al. (2020). First we predict the arrival time of earthquakes
273   with $M_S/M_W \geq 4.5$ using the International Seismological Centre (ISC) catalog where the
274   Rayleigh wave time window is taken from 20 s before a predicted 4.0 km s^{-1} arrival to 600 s after
275   it, and exclude any time windows that overlap with the Rayleigh wave windows. Then we check
276   the remaining time windows in an earthquake band (10-40 s) and remove those with suspicious
277   high amplitudes (either small earthquakes or signal singularities). Furthermore, the remaining
278   time windows are then evaluated using a norm outlier rejection method (Janiszewski et al.,
279   2019). In this way, the selected time windows will contain purely noises. To avoid over-
280   corrections that would distort the signals, we follow Ye Tian and Ritzwoller (2017) and only
281   apply corrections for periods where the transfer function coherence is above 0.4, which mostly
282   lies in a period range between 15 and 150 s. After removing the tilt and compliance noise, the
283   surface wave signals extracted from both ambient noise cross-correlations and teleseismic
284   earthquakes are distinctly improved (Figure S1 in the Supporting Information).

285   3.3 Ambient noise tomography

286   With the data of all land stations and pre-processed OBSs, the interstation empirical
287   Green's functions are then determined by ambient noise cross-correlation procedures described
288   in Bensen et al. (2007). First we cut the continuous data to daily length and down-sample them to
289   one sample per second. Then we calculate the ambient noise cross-correlations over the vertical-
290   vertical components of daily length time series using both time-domain normalization with an

291 earthquake filtering band of 10-40 s and spectral whitening. Daily cross-correlations are stacked
292 for each station pair over the entire time period of the deployment.

293   We then apply an automated Frequency-Time Analysis (FTAN) with a phase-matched
294 filter to measure the Rayleigh wave phase and group velocity dispersion curves from the
295 symmetric Green's functions of each station pair (Bensen et al., 2007; Lin et al., 2008). As there
296 are rapid changes from oceanic to continental structures, the FTAN measurements for land-land
297 station pairs, OBS-land station pairs, and OBS-OBS pairs also vary a lot (Figure S2 in the
298 Supporting Information). The oceanic paths generally show extremely low group/phase velocity
299 at periods < 16 s but increase rapidly to high velocity at periods > 20 s.

300   There are relatively few good measurements below 8 s, and the signal-to-noise ratio
301 (SNR) decreases rapidly for oceanic paths at periods greater than 36 s, thus we invert for phase
302 and group velocity maps from 8 to 36 s using a Gaussian ray-theoretical tomography method
303 (Barmin et al., 2001). The grid spacing is 0.3° × 0.2°, which is roughly equally spaced in
304 longitude and latitude. The isotropic cell size in the tomographic inversion is 0.5°, which could
305 recover checker sizes ranging from 3°×2° to 1.8°×1.2° in checkerboard tests (Figure S3 in the
306 Supporting Information).

307   For each frequency, we only keep station pairs with distances larger than twice the
308 wavelength. To exclude the unreliable measurements while considering the relatively high noise
309 of OBS records, we excluded measurements with SNR < 7. To further constrain the 2-D
310 inversion results, we apply quality control based on the travel-time residuals from the previous
311 inversion. The paths with residuals outside two standard deviations, about 2 % to 6 % of the total
312 measurements for each period, are removed after three times of quality control. The remaining
313 measurements are used to finalize the Rayleigh phase and group velocity maps from 8 s to 36 s
314 (Figure S4 in the Supporting Information). At short periods (between 8 to 14 s), the group and
315 phase velocity maps reflect the very shallow structure and water depth, where incoming plate
316 and trench are dominated by low-speed anomalies and mountain ranges show high-speed
317 anomalies. At longer periods (20-30 s), the group and phase velocity maps reflect the crust and
318 uppermost mantle structure, where the incoming plate is dominated by high-speed anomalies and
319 low-speed anomalies cover the forearc region. The similar patterns between 20 s phase velocity
320 and 30 s group velocity illustrate that at the same frequency, the phase velocity is sensitive to
321 deeper structures than group velocity.

322 3.4 Teleseismic earthquake tomography

323   At longer periods (T > 20 s), we analyze the Rayleigh wave phase velocity from
324 teleseismic waves traversing the array using the Helmholtz tomography method (Lin &
325 Ritzwoller, 2011) implemented in the ASWMS package (Jin & Gaherty, 2015). We select
326 earthquakes with $M_W \geq 5$ and epicentral distances between 20° and 160° from the International
327 Seismological Centre (ISC) catalog for analysis. The events are chosen to be high-quality,
328 relatively evenly distributed with respect to the seismic array, and also separated enough in time
329 from each other to avoid overlapping on seismograms. Finally, 265 earthquakes with high SNR
330 are used to determine the phase velocities.

331   The implementation of Helmholtz tomography involves an Eikonal tomography plus the
332 amplitude term correction, where Eikonal tomography inverts the phase delays for spatial

333 variations in apparent phase velocity via the Eikonal equation (Lin et al., 2009) and amplitude
334 term correction accounts for the local amplification due to wavefield focusing and defocusing
335 effects (Lin et al., 2012; Eddy & Ekström, 2014; Russell & Dalton, 2022). The waveforms of all
336 events and stations are cut from the earthquake origin time to 10800 s after. Based on
337 multichannel cross-correlations of station pairs within 410 km, the phase velocity variations of a
338 series of periods are estimated for each event at node spacing $0.3° × 0.2°$. We estimate the local
339 amplification term (Eddy & Ekström, 2014), calculate the smoothed Laplacian term of corrected
340 2-D amplitudes, and finally convert the apparent phase velocity to structural phase velocity for
341 each period. The final structural phase velocity dispersion maps are stacked over maps of all
342 events. The checkboard tests suggest the above parameters work well to recover the input
343 anomalies (Figure S5 in the Supporting Information).

344   The tomographic results produce isotropic phase velocity at node spacing $0.3° × 0.2°$ for
345 periods from 23 s to 100 s (Figure S6 in the Supporting Information). The phase velocity maps at
346 these longer periods constrain the lower crust and uppermost mantle structure. At the 40 s period,
347 the high-velocity anomalies still dominate the incoming plate region, and also extend north
348 across the Aleutian Trench a little bit compared to the 25 s phase velocity map. At even longer
349 periods (e.g., 60 s, 100 s), the trench region is replaced by low velocity, and high-speed
350 anomalies gradually occupy the volcanic arc.

351 3.5 Local Rayleigh wave dispersion curves

352   The Rayleigh wave phase velocity dispersion curves measured from ambient noise and
353 earthquake data are then evaluated in their overlapping period band. Comparisons between the
354 phase velocity maps show that their measurements are generally consistent at 24-34 s periods.
355 For example, at 30 s, most of the phase velocity differences are less than 0.1 km s^{-1} (Figure 3).
356 The incoming plate, trench, and northern Bristol Bay area generally have slightly higher phase
357 velocity from ambient noise tomography than from earthquake tomography, whereas other areas
358 show the opposite relationship (Figure 3). Furthermore, we define the reliable range of nodes to
359 extract local dispersion curves as those with high ray path coverage in both ambient noise

360   tomography and teleseismic earthquake tomography, as well as small phase velocity differences
361   in their overlapping phase velocity maps.
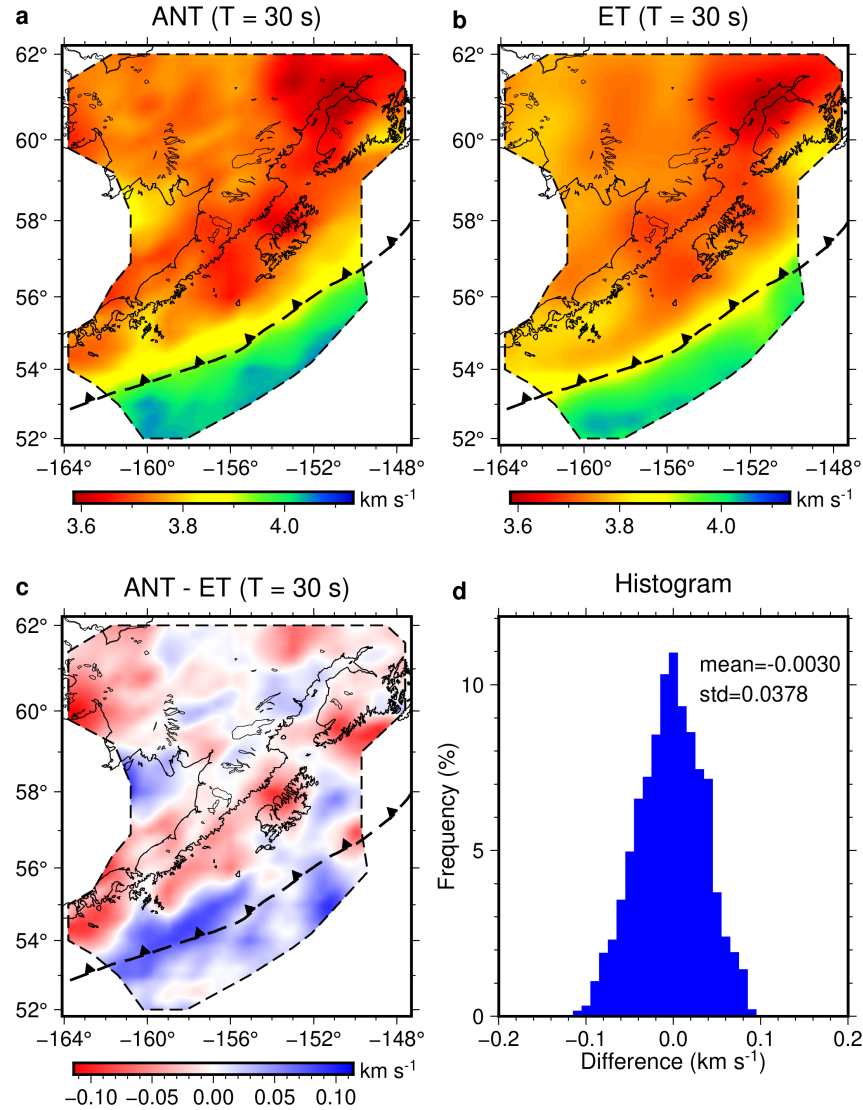
362

363

364   **Figure 3**. Comparison of Rayleigh wave phase velocity at 30 s period of the study region
365   estimated from ambient noise tomography (ANT) and earthquake Eikonal tomography (ET). **(a)**
366   The phase velocity map at 30 s from ANT. **(b)** The phase velocity map at 30 s from ET. **(c)** The
367   difference between phase velocity maps from ANT and ET at 30 s. **(d)** Histogram of the
368   differences in (c), showing that the results from the two tomography results are generally less
369   than 0.1 km s^{-1}.

370

371   Therefore, the final phase velocity dispersion curves for each node are constructed in the
372   following way: 1) For periods less than or equal to 23 s, the phase velocities come from ambient

373 noise tomography. 2) For periods greater than or equal to 36 s, the phase velocities come from
374 Eikonal tomography. 3) For periods larger than 23 and less than 36 s, we take a weighted
375 average of the measurements from the two methods, with the weights changing linearly in
376 between.

377   Uncertainty estimation of the local phase and group velocity curves constructed above is
378 essential and important for the shear velocity inversion. The above two tomographic methods
379 used here neither provide an estimation of uncertainties directly, but we can estimate the local
380 uncertainties for short periods from the local resolution in the method of Barmin et al. (2001),
381 where the uncertainties of phase velocity are normalized for each period so that the uncertainty
382 of data-rich region is 0.027 km s^{-1} for 8 s, 0.021 km s^{-1} for 16 s, 0.016 km s^{-1} for 24 s, 0.021 km
383 s^{-1} for 32 s, 0.024 km s^{-1} for periods > 32 s. Uncertainties for other periods are interpolated based
384 on these anchor points. From an empirical relationship, the uncertainties of group velocity are
385 estimated to be twice that of phase velocity (e.g., Shen et al., 2016). Considering that the group
386 velocity measurements in this region have even larger uncertainty at shorter periods, we use a
387 factor of 2.5 to calculate the group velocity uncertainties. The local uncertainties of phase
388 velocity from the Helmholtz tomography are scaled from the corresponding standard deviation
389 values by multiplying a factor of 0.3. In this way, the phase velocities from two datasets at
390 overlapped periods have similar uncertainties.

391 3.6 P-wave receiver functions for land stations

392   Contrasting to the surface wave analysis that requires a concurrent deployment of seismic
393 stations, the P-wave receiver functions (PRFs) analysis is performed on each station individually.
394 To use joint inversion to better constrain the continental Moho, we try to include all land stations
395 within the study region that operated sufficient dates from May 2014 to December 2021. The
396 longer date range is chosen to make the best use of TA stations and other temporary stations with
397 enough data outside the AACSE deployment period. For all land stations with sufficient data
398 quantity and quality, we first prepare the P-wave seismic data from earthquakes with $m_b \geq 5.0$
399 and epicentral distances between 30° and 90°. The seismograms are decimated to a sample rate
400 of 10 Hz and cut to a time window from 30 s before and 60 s after the P-wave onset. The
401 horizontal components are cosine tapered and pre-filtered with a bandpass filter of 0.02 to 2 Hz,
402 then rotated into radial and transverse components. Using a time-domain iterative deconvolution
403 algorithm (Ligorría & Ammon, 1999), we perform 200 iterations to estimate the PRFs, using a
404 Gaussian low pass filter with a corner frequency of ~1 s.

405   After applying an automated quality control based on the individual PRFs and the
406 similarity of PRFs over the range of back-azimuths, we generally retain more than 30 PRFs for
407 each station. If the individual PRFs reach a good azimuthal coverage, a "harmonic stripping"
408 method is applied to determine the isotropic PRF, which represents the common component over
409 all azimuths (Shen et al., 2013). For stations lacking a good azimuthal distribution of individual

410   PRFs, we use a weighted stack of all PRFs to get a single PRF for the station site. In total, we
411   obtain 188 land stations with quality-controled stacked PRFs.

412   3.7 Bayesian Monte Carlo inversion

413   The resulting local Rayleigh wave dispersion curves with group velocity from 8-36 s and
414   phase velocity from 8-100 s are then inverted for the azimuthally averaged vertically polarized
415   shear wave velocity (V_{SV}) structure using a Bayesian Monte Carlo inversion method (Shen et al.,
416   2013; Shen & Ritzwoller, 2016). The Bayesian inversion requires the proper construction of the
417   model space and the estimation of prior information, which is based on the location of the nodes.
418   We divide the nodes into three groups: the incoming plate group to the south of the trench axis,
419   the inner trench slope group just north of the trench axis, and the forearc and backarc group. The
420   boundary between the inner trench slope and the forearc/backarc region is taken as the 20 km
421   depth contour of the slab interface from Slab2.0 model (Hayes et al., 2018).

422   For the nodes in the ocean, we include a water layer with a starting thickness from the
423   125-km Gaussian-filtered bathymetry (m_{w0}) and allow a 100% thickness but no more than 1.5
424   km perturbation. The incoming plate nodes include a 0-1 km sedimentary layer in the Shumagin
425   segment and a 0-2 km sedimentary layer in the Semidi and Kodiak segments, based on the
426   previous active-source results (Shillington et al., 2015). For inner trench nodes, the starting
427   crustal thickness of (m_{c0}) is calculated following the depth of slab interface as well as the slab
428   dip angle in Slab2.0 model, with an assumption of a 6 km oceanic crust atop the subducting slab.
429   The crustal thickness of most nodes in the inner trench slope region then allows a 30% thickness
430   perturbation with respect to m_{c0}. One exception is the Kenai Peninsula nodes, which have a slab
431   interface less than 20 km in the Slab2.0 model, but tend to have a deeper Moho than that
432   predicted by the slab interface through tests. We thus allow those nodes within the Kenai
433   Peninsula to have a 60% thickness perturbation with respect to m_{c0}. For all nodes, the uppermost
434   mantle structure from the Moho discontinuity down to 300 km depth is represented by a 6-knot
435   B-spline curve. The bottom 100 km is gradually merged into the STW105 V_{SV} model
436   (Kustowski et al., 2008). The specification of the prior distribution of models is defined by a

437 series of variables for three groups of nodes in different regions (Table 1). Each variable in
438 different regions is set accordingly based on our a priori information the study region.

439

440 Table 1. Specification of the prior distribution of models in different regions.
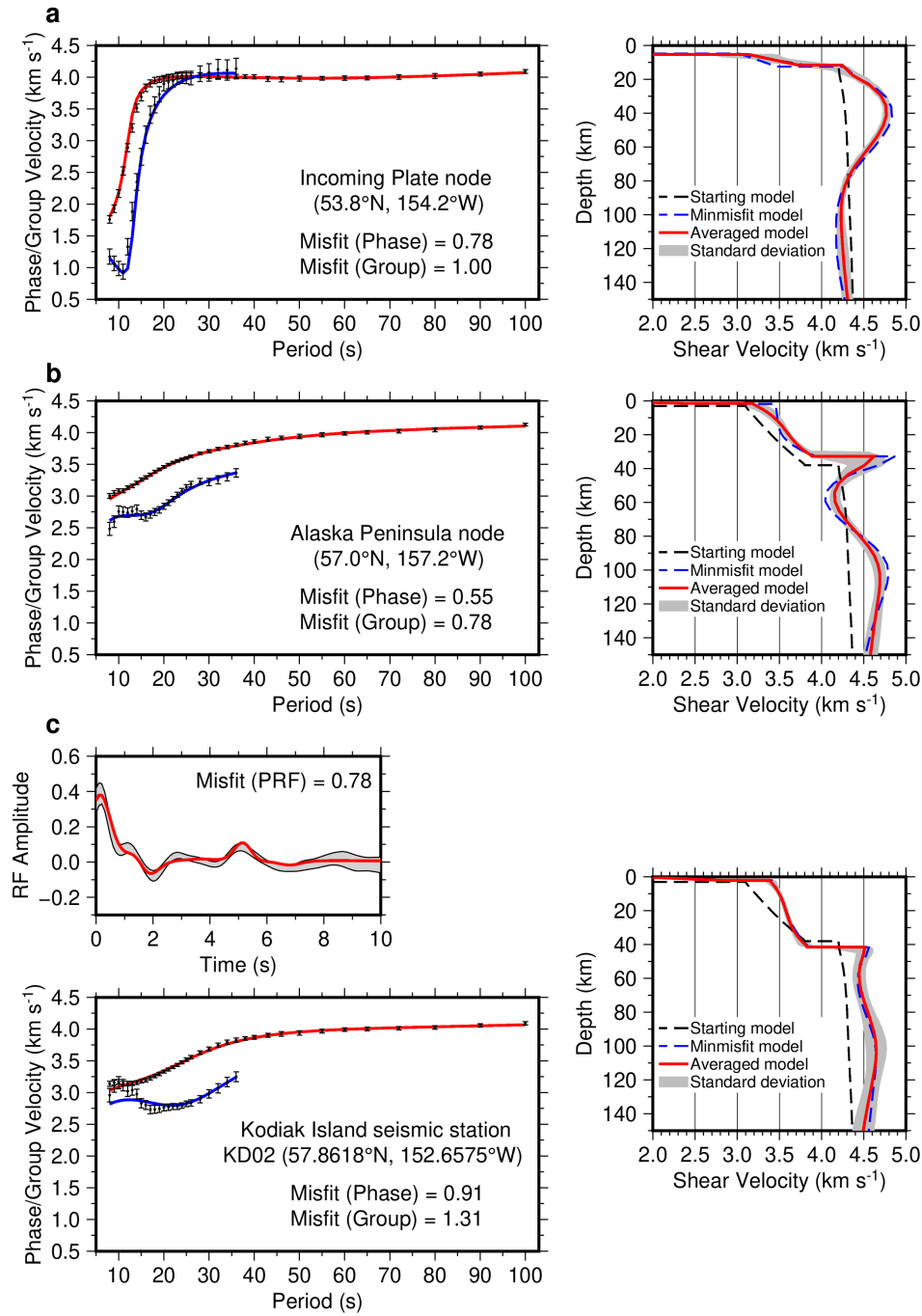
		Incoming plate	Inner trench slope	Forearc and backarc
Water layer (for oceanic nodes only)	Thickness	$m_{w0} \pm \min(m_{w0}, 1.5)$ (km)		
Sedimentary layer	Thickness	Shumagin: 0-1 km Semidi & Kodiak: 0-2 km	0-6 km	0-6 km
	V_{SV} (top: 1.0 km s^{-1}; bottom: 2.0 km s^{-1})	Linear velocity increase, with top and bottom allows 1.0 km s^{-1} and 1.5 km s^{-1} perturbation, respectively		
Crustal layer	Thickness	4-8 km	For nodes within Kenai Peninsula: $m_{c0} \pm 0.6\, m_{c0}$ (km) For others: $m_{c0} \pm 0.3\, m_{c0}$ (km)	20-50 km
	V_{SV} (top: 3.1 km s^{-1}; bottom: 3.8 km s^{-1})	Linear velocity increase, both variables allow 20% perturbation	3 cubic B-spline coefficients, each allows 20% perturbation	4 cubic B-spline coefficients, each allows 20% perturbation
Mantle layer	V_{SV} (top: 4.2 km s^{-1}; bottom: 4.4 km s^{-1})	6 cubic B-spline coefficients, each allows 25% perturbation		

441

442   The Bayesian Monte Carlo inversion is performed with a grid of 0.3° × 0.2° spaced nodes
443 which have phase and group velocity measurements from both ambient noise data and
444 teleseismic earthquake data. Examples of inversion results show that the Bayesian Monte Carlo
445 inversion can well fit the measured group and phase velocity dispersion curves (Figure 4a;

446 Figure 4b). Finally, all 2015 evenly spaced nodes give structures that are based on the mean of
447 at least 5000 acceptable models.

448 For land stations with high-quality PRFs, their local structures at stations are jointly
449 determined using the Rayleigh wave dispersion and PRFs. The Moho conversion in the PRF
450 between 3 and 7 s is very helpful to invert the Moho depth and resolve potential trade-offs
451 between Moho depth and velocity structure (Figure 4c). Among all 188 stations with high-
452 quality PRFs, we finally get 180 well-constrained joint inversion results and their structures are
453 generally based on the mean of at least 500 acceptable models. The 3-D structural model is
454 constructed on the grid of evenly spaced nodes by combining the structure from the Rayleigh
455 wave inversion with the PRF joint inversion results for all well-constrained stations within a 75
456 km distance, using an inverse distance weighting scheme (Shen et al., 2018). The structure for
457 nodes lacking nearby land seismographs with good PRF results is based solely on the Rayleigh
458 wave inversion results. The final 3-D azimuthally-averaged vertically-polarized shear velocity
459 model is determined using all the well-constrained nodes by interpolating with a simple kriging
460 algorithm (Shen & Ritzwoller, 2016; Shen et al., 2018).

461

462

Figure 4. Examples of the Bayesian Monte Carlo inversion for different geological regions show the resulting 1-D shear wave velocity structure beneath each node and how the predicted phase and group dispersion curves (and receiver function, if applicable) fit the measurements. **(a)** Incoming plate node (53.8°N, 154.2°W). The derived V_{SV} profile is an oceanic structure with reduced velocity in the uppermost mantle. (b) Alaska Peninsula node (57.0°N, 157.2°W). The derived V_{SV} profile is a typical volcanic arc structure with a low-velocity zone (LVZ) beneath

469   the Moho. **(c)** Joint inversion result for Kodiak Island seismic station KD02. The structure shows
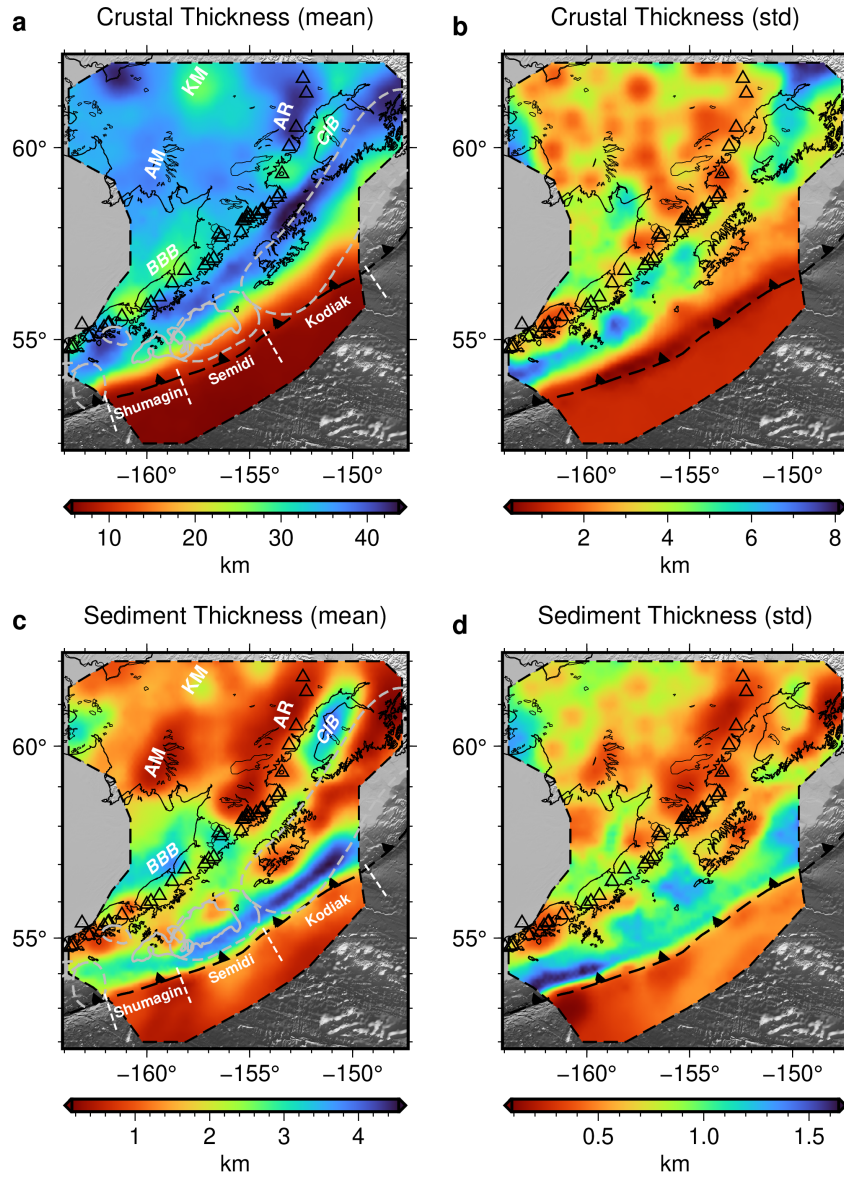470   a thick, low-velocity crust and a strong subducting oceanic Moho discontinuity.

471

4 Results

473   4.1 Thickness of crust and sediment

474   The posterior distribution of the crustal thickness and sediment thickness provides their
475   preferred values and uncertainty maps (Figure 5). Note that the actual forearc structure is rather
476   complex as there are possibly two Moho discontinuities (an overriding plate Moho and a
477   subducting plate Moho), but we only set one Moho in the parameterization since the resolution
478   of the methods does not allow for reliably determining a complex structure. Therefore, the
479   observed Moho in the seaward part of the forearc represents the subducting plate Moho and the
480   observed Moho in the arcward section of the forearc represents the overriding plate Moho, with a
481   section in between where the overriding and subducting Mohos are in close proximity and the
482   identity of the Moho discontinuity from the inversion is uncertain. The thickest crust is a band in
483   the inner forearc from the Kodiak segment to the eastern edge of the Shumagin segment, whose
484   crustal thickness exceeds that in the arc and backarc regions (Figure 5a). The corresponding
485   uncertainty map shows how joint inversions with PRFs help reduce the uncertainty of crustal
486   thickness (Figure 5b). The crustal thickness along the arc is relatively constant, consistent with
487   results from a previous receiver function analysis of the stations along the Aleutian island arc
488   (Janiszewski et al., 2013).

489   Sediment as defined in this study includes both recent pelagic and terrigenous sediment
490   as well as deformed and potentially older sediments in forearc basins and in the accretionary
491   prism. The mean distribution of sediment thickness is generally less than 2 km in the incoming
492   plate and the continental regions. Though the inversion method is not highly sensitive to thin
493   sedimentary cover, the model clearly resolves thicker sediment along the outer forearc of the
494   Kodiak and Semidi segments and in the Bristol Bay and Cook Inlet basins. The very thick (up to
495   4.5 km thickness) low-velocity sediments in the outer forearc basin (Figure 6a) are consistent
496   with the outer forearc basin structure in the Shumagin segment (Shillington et al., 2022) and to
497   the south of Kodiak Island (Fisher & von Huene, 1982) determined using active source methods,
498   though thickest sediments of Shillington et al. (2022) are in the accretionary prism. Bristol Bay
499   Basin and the Cook Inlet Basin both show about 3 km of low-velocity sediments. The
500   distribution of sediment thickness in the Cook Inlet Basin has a similar pattern to the map of
501   depth to the base of Cenozoic strata (Shellenbaum et al., 2010; Silwal et al., 2018). The previous
502   active-source survey in Bristol Bay Basin shows a boundary at about 3 km depth for the faulted
503   basement (Walker et al., 2003), consistent with the sediment thickness results here.

504

Figure 5. Map views of the posterior distribution for the crustal thickness and sediment thickness of the study region. The background image is the topography/bathymetry in gray scales. **(a)** Map view of the mean of the crustal thickness. The dashed gray lines are the contours of earthquake rupture zones shown in Figure 1b. The dashed white lines marked the range of Shumagin, Semidi, and Kodiak segments. Annotation of geological features: AM = Ahklun Mountains; KM = Kuskokwim Mountains; AR = Alaska Range; BBB = Bristol Bay Basin; CIB = Cook Inlet Basin. **(b)** Map view of the uncertainty of the crustal thickness. **(c)** Map view of the mean of the sediment thickness. Other labels are the same as that in (a). **(d)** Map view of the uncertainty of the sediment thickness.

515

516   4.2 Shear velocity structure

517   The shear wave velocity structure is presented as a series of map views (Figure 6) as well
518   as cross-sections normal to the trench along the Shumagin, Semidi, and Kodiak segments (Figure
519   7). The downgoing Pacific plate, featured by high velocity in the mantle, dominates the shear
520   velocity model. The continuous high-velocity zones clearly depict the depth of the upper
521   interface of the subducting slab, which changes from less than 10 km near the trench to greater
522   than 100 km beneath the volcanic arc, similar to the slab geometry from previous studies (e.g.,
523   Abers et al., 2017). The uppermost mantle beneath the incoming plate shows a clear velocity
524   reduction from the seaward end to the near-trench region (Figure 7).

525   The 3-D shear velocity model successfully resolves features like the accretionary prism,
526   forearc crust, shallow basins, arc volcanic magma, and major mountains. At very shallow depths
527   (~5 km), the outer forearc is dominated by low-velocity sediment of the accretionary prism while
528   most regions show a typical crystalline upper crust (Figure 6). In Semidi and Kodiak segments,
529   the outer forearc shows a low-velocity (~3.5 km/s) lower crust with larger thickness, which is not
530   found in the Shumagin segment. A very similar contrast is also seen in recent active-source
531   imaging, where results show a lower velocity crust in the Semidi segment than that in the
532   Shumagin segment (Burstein et al., 2022). The Bristol Bay Basin is featured by thinner crust,
533   high-velocity lower crust, and low-velocity upper mantle. The low-velocity anomalies beneath
534   volcanic arcs are observed for all segments but are most prominent in the Kodiak segment
535   (Figure 7). The Ahklun Mountains and Kuskokwim Mountains show similar crustal velocities
536   but quite different Moho depths and upper mantle structures (Figure 5; Figure 7).
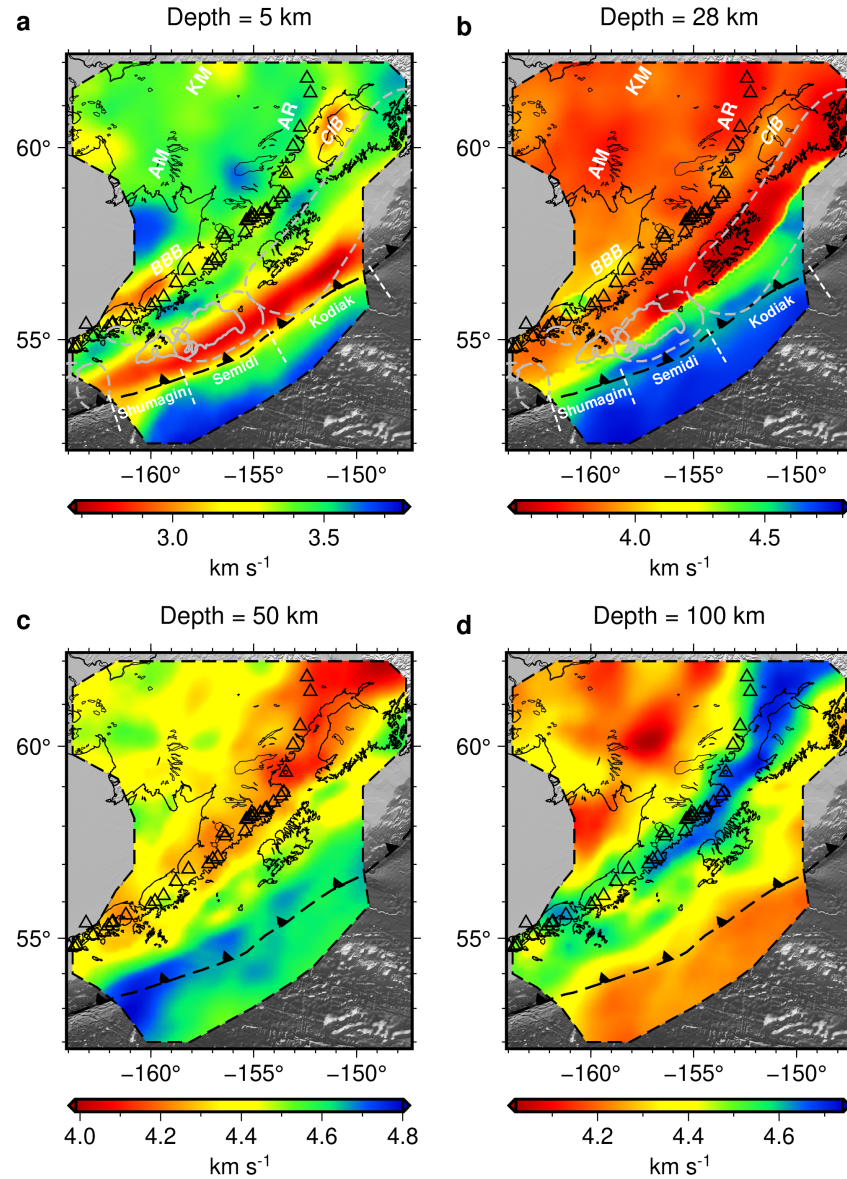
537

538

Figure 6. Horizontal slices for azimuthal averaged shear wave velocity (V_{SV}) of the study region
at different depths. The background image is the topography/bathymetry in gray scales. **(a-d)**
Map view of the shear velocity at 5, 28, 50, and 100 km depths, respectively. The depth is
defined here as relative to the solid surface, either the seafloor or the continental surface. Active
volcanoes are marked as triangles along the volcanic arc. Note that there are different velocity
color scales for each sub-figure. In (a) and (b), the dashed gray lines are the contours of
earthquake rupture zones shown in Figure 1b and the dashed white lines marked the range of
Shumagin, Semidi, and Kodiak segments. Annotation of geological features: AM = Ahklun
Mountains; KM = Kuskokwim Mountains; AR = Alaska Range; BBB = Bristol Bay Basin; CIB
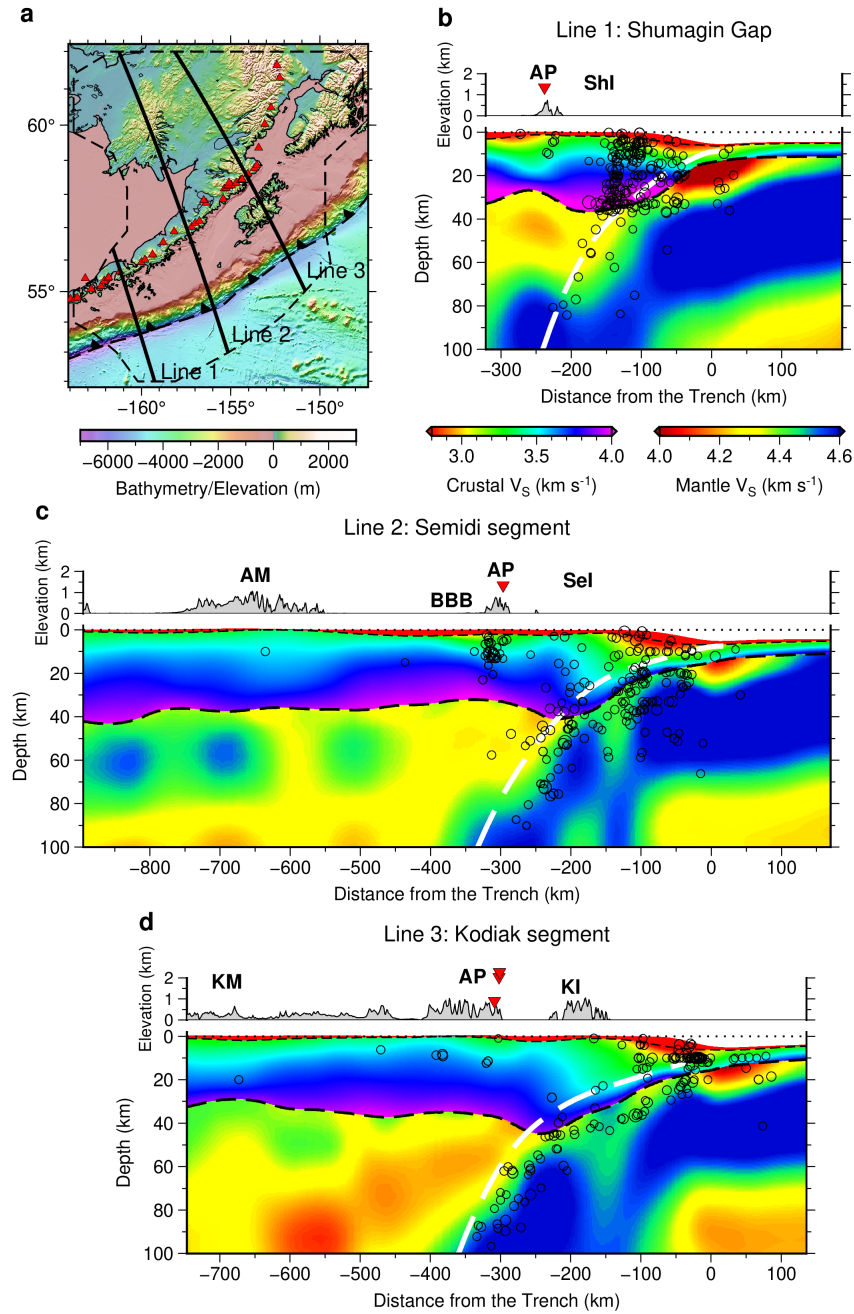= Cook Inlet Basin.

549

Figure 7. Vertical cross-sections of the 3-D shear velocity model along three lines crossing the Shumagin, Semidi, and Kodiak segments, respectively. **(a)** Location of the three lines shown on the bathymetry and elevation map. The arc volcanoes are plotted as red triangles. Dashed black line encloses the study region. **(b-d)** Cross-sections along each line. The x-axis is the distance relative to the trench axis with a positive distance in the direction of the incoming Pacific plate. The elevation along the profile is plotted above the velocity image with geological features labeled (Annotation: AP = Alaska Peninsula; AM = Ahklun Mountains; KM = Kuskokwim Mountains; BBB = Bristol Bay Basin; ShI = Shumagin Islands; SeI = Semidi Islands; KI = Kodiak Island). Active volcanoes near the profiles (within 25 km) are plotted as red triangles, above the topography image. The V_{SV} images show the structure along each cross-section, where

561 V_{SV} values in the crust and mantle use different color bars. Depths are plotted relative to sea
562 level here (shown as a black dotted line). The thin black dashed line is the boundary between
563 sediment and crust, while the thick black dashed line is the Moho depth in the 3-D V_{SV} model.
564 The white dashed line depicts the depth of the slab interface from Slab2.0 (Hayes et al., 2018).
565 The M ≥ 4 earthquakes from the AEIC catalog since 1990 and the AACSE catalog (Ruppert et
566 al., 2022) are plotted on the cross-section image as open black circles if they are within 50 km
567 from the projection line.

568

5 Discussion

570 The 3-D shear velocity images clearly reveal systematic along-strike variations in the
571 subduction zone structure. Here we will focus on the predominant features, discussing the
572 incoming plate hydration, the forearc crustal thickness, and the backarc basin structure.

573 5.1 Thick forearc crust associated with the Chugach Terrane

574 The crustal structure of the forearc shows a band of thick crust (35-42 km) extending
575 from the eastern edge of the study region, beneath Kodiak Island, to just east of the Shumagin
576 Islands. Crustal thickness in this region generally exceeds the crustal thickness of the volcanic
577 arc and backarc regions (Figure 5a). Immediately seaward of the thickest crust, the velocity
578 profile is characterized by a thick section of reduced lower crustal velocities (~3.5 km s^{-1})
579 extending to the plate interface at depths of about 30 km at many locations. This feature may be
580 the along-strike continuation of the 20-km-thick low velocity lower crustal units imaged just to
581 the east of Kodiak Island by the EDGE active source study (Ye et al., 1997). The shear velocities
582 in this study are consistent with the lowermost crustal P wave velocity of about 6.0 km s^{-1}
583 observed by Ye et al. (1997). They interpreted the low-velocity region as underplated sediments
584 and upper crustal rocks of subducted terrains, associated with the uplift of the Kodiak region
585 during the Eocene to Oligocene (Moore et al., 1991). An alternative interpretation is that those
586 lower velocities represent the Paleogene-aged Prince William Terrane and/or the Mesozoic-aged
587 Chugach Terrane (e.g., Horowitz et al., 1989); these terranes are dominately composed of lightly
588 metamorphosed accretionary complexes (e.g., Sample & Moore, 1987), which would also be
589 expected to have relatively low velocities. In this case, the reflections observed by Moore et al.
590 (1991) may arise from layering within Prince William/Chugach/Peninsula Terranes from
591 accretionary complexes or intrusions. Intracrustal reflections are observed on all the
592 Alaska/Aleutian arc profiles and bright bands of lower crustal reflections are even observed
593 farther west in the oceanic part of the arc (Calvert & McGeary, 2013). However, these studies
594 did not show a clear anticlinal structure as described by Moore et al. (1991) and Ye et al. (1997).

595 The results presented here suggest that the distinctive thickened crust just inboard of the
596 slow lower crustal forearc material extends to the eastern edge of the Shumagin Islands region.
597 The Chugach Terrane is often thought to extend to Sanak Island west of the Shumagin Islands
598 due to the similarity of the accretionary and intrusive surficial rocks (e.g., Bradley et al., 2003).
599 However, crustal thickness becomes variable within and westward of the Shumagin Islands
600 region, being reduced in places to about 30 km, and the lower crust has a higher velocity (~3.9
601 km s^{-1}) beneath the Shumagin Islands. Thus the Shumagin islands may represent a major change
602 in forearc morphology, defining a transition from thick accretionary crustal material and thicker
603 forearc crust to the east to more conventional forearc crust to the west. Alternatively, the forearc

604 crust in the Shumagin region may have been thinned and modified by deformation at the edge of
605 the Beringian margin that lead to the formation of a series of extensional basins in this region in
606 the Oligocene-Miocene (e.g., Horowitz et al., 1989; Bécel et al., 2017; von Huene et al., 2019;
607 Kahrizi et al., 2024).

608   The along-strike and down-dip variations in the thickness and velocity of the forearc
609 crust above the megathrust could be important for the mechanical properties of the megathrust,
610 with implications for strain accumulation and release (Sallarès & Ranero, 2019; Bassett et al.,
611 2022). Although the recent 2020 M7.8 Simeonof and 2021 M8.2 Chgnik earthquakes occurred at
612 similar depth ranges in the Shumagin and Semidi forearc regions (e.g., Liu et al., 2023), the
613 differences in crustal thickness along strike suggest that rupture zone of the 2021 M8.2
614 earthquake in the Semidi segment is overlain by continental crust, but that part of the rupture
615 zone of the 2020 M7.8 in the Shumagin segment may have occurred below the continental Moho
616 (Shillington et al., 2022) (Figure 5a, Figure 7); complexity of megathrust properties near the
617 continental Moho are speculated to contribute to the patchiness of the M7.8 event (Shillington et
618 al., 2022; Liu et al., 2023). In the Semidi segment, recent rupture in the 2021 M8.2 event is
619 confined to depths of ~26-42 km (Liu et al., 2023), the portion of the megathrust overlain by
620 relatively high-velocity crust (e.g., Figure 7c). The shallower megathrust overlain by low-
621 velocity crust has recently been observed to host a slow slip event in 2018 and aseismic aftership
622 following the 2021 event (Brooks et al., 2023; He et al., 2023). These correlations suggest that
623 the overriding plate plate could influence megathrust slip behavior. Downdip changes in bulk
624 rigidity or permeability of the overriding plate and/or in frictional properties on the megathrust
625 due to the overriding plate are proposed to influence megathrust behavior in other locations
626 (Sallarès & Ranero, 2019; Bassett et al., 2022). Finally, differences in overriding plate structure
627 and present-day inputs to the subduction zone could also influence megathrust frictional
628 properties and heterogeneity. Low velocities in the outer forearc of the Semidi and Kodiak
629 segments shown here could indicate significant underplating in the past (Moore et al., 1991), and
630 thicker sedimentary sections are subducting in these segments today than farther west (e.g., von
631 Huene et al., 2012; J. Li et al., 2018). Extensive sediment subduction is likely to reduce the
632 inherent roughness of the plate interface and produce a large, smooth megathrust fault zone
633 favorable to great earthquakes (Bangs et al., 2015; Scholl et al., 2015). Global studies suggest
634 higher seismic coupling and propensity for great earthquakes in regions with substantial
635 sediment subduction and underplating (Ruff, 1989; Heuret et al., 2012).

636 5.2 Volcanic arc and backarc structure

637   The mantle wedge structure is characterized by low shear velocities (4.1-4.3 km s^{-1}) in
638 the upper mantle beneath the volcanic arc. The Kodiak and Semidi segments have adequate
639 resolutions in the backarc and both reveal continuous low-velocity anomalies sloping upward
640 from more than 100 km depth beneath the backarc to the Moho beneath the volcanic front
641 (Figure 7). Similar inclined low-velocity zones have been observed at many volcanic arcs around
642 the world, and are generally interpreted as the zone of hydrous partial melting and melt transport
643 above the slab (e.g., Zhao et al., 2007; Wiens et al., 2008). These results suggest that a
644 significant portion of the partial melt formation in the Alaska mantle wedge occurs beneath the
645 backarc rather than immediately beneath the volcanic arc. Melt is transported along the inclined
646 zone by porous and channelized flow to the Moho beneath the volcanoes (Wilson et al., 2014;
647 Cerpa et al., 2018).

648   Unlike for some arcs, identified in the compilation of Abers et al. (2017), there is no
649 indication of a high-velocity mantle wedge seaward of the volcanic arc. Instead, low mantle
650 velocities extend seaward from the volcanic front into the corner of the mantle wedge (Figure 7).
651 Partial melt does not provide a good explanation for these low velocities, since melt is highly
652 buoyant and there is no magmatism observed on the forearc side of the volcanic front. In
653 addition, heat flow anomalies characteristic of magma supply to the crust are limited to the
654 volcanic arc and backarc regions in most arcs (Furukawa, 1993; Rees Jones et al., 2018). The
655 low velocities in the wedge corner instead could result from serpentinization of the mantle
656 peridotite by water released from the slab immediately below (Hyndman & Peacock, 2003;
657 Reynard, 2013). The reduced shear wave velocities in the wedge corner of 4.1-4.2 km s^{-1} are
658 compatible with P-wave velocities of 7.3-8.0 km s^{-1} from P-wave tomography in the Shumagin
659 region (Abers, 1994). Assuming the serpentine is lizardite, the shear velocity of ~4.1 km s^{-1}
660 indicates roughly 19 vol% mantle serpentinization above the slab in the wedge corner. The
661 resolution is insufficient to constrain any along-strike variation of mantle wedge serpentinization.

662   The backarc crust shows significant along-strike variations. In the northeast part of the
663 study region, the backarc is characterized by a relatively typical continental crust with a
664 thickness of about 35 km. However, in southern Bristol Bay, crust with significantly reduced
665 thickness (~28 km) is found just to the north of the Alaska Peninsula and the active volcanic arc
666 (Figure 5a). The entire region of Bristol Bay is underlain by a 15 km thick layer of high velocity
667 (~3.9 km s^{-1}) lower crust (Figure 7c). The high-velocity lower crust indicates a dense mafic
668 composition, resulting in a crust with a higher average density. Isostatic compensation of this
669 denser and in some places thinner crust could contribute to lower elevations in Bristol Bay
670 relative to backarc regions farther to the northeast.

671   Active-source surveys have shown a significant sedimentary sequence in the Bristol Bay
672 Basin (Marlow et al., 1994; Walker et al., 2003). Bond et al. (1988) suggested that the basin
673 formed primarily by flexural subsidence caused by the Oligocene to present crustal thickening of
674 the Alaska Peninsula. In contrast, Walker et al. (2003) proposed that the basin was initially
675 formed by extension. In the Walker et al. (2003) model, an early or middle Eocene through late
676 Miocene phase of extension lead to fault-controlled subsidence, then a late Eocene through
677 Holocene phase of volcanic-arc loading or northward prograding delta lead to flexural
678 subsidence. Our observation of the thinner crust with a dense high-velocity mafic lower crust
679 beneath the Bristol Bay basin supports models proposing that the basin originally formed
680 through tectonic extension.

681 5.3 Incoming plate hydration

682   The incoming plate structure clearly shows a low-velocity zone at the top of the
683 subducting oceanic mantle (Fig. 6). The velocities decrease towards the trench and show
684 significant along-strike variations. Low-velocity zones at the top of the incoming plate mantle
685 have been observed at many other subduction zones and are generally attributed to the
686 serpentinization of mantle peridotite (Ivandic et al., 2008; Van Avendonk et al., 2011;
687 Shillington et al., 2015; Cai et al., 2018; Mark et al., 2023) and/or to the effects of water in plate-
688 bending faults (Miller & Lizarralde, 2016; Korenaga, 2017). The Shumagin segment shows a
689 distinct low-velocity zone (~3.65 km s^{-1}) at the top of the incoming plate mantle, suggesting
690 strong hydration if the velocity reduction is due to serpentinization. In contrast, the Semidi

691 segment and Kodiak segment show much weaker hydration of the incoming Pacific plate, with a
692 velocity reduction only to ~4.05 km s^{-1} and ~4.0 km s^{-1}, respectively.

693   The extent of incoming plate hydration can be better compared using velocity profiles at
694 locations near the trench axis (Figure 8). Since the resolution of the incoming plate in the Kodiak
695 segment is limited by the small number of nearby OBSs returning data, we only make the
696 comparison between the Shumagin segment and the Semidi segment. We choose the trench
697 profiles of both Shumagin and Semidi segments at locations 20 km seaward from the trench axis
698 to limit the smoothing effect of surface waves. To evaluate the magnitude of mantle hydration,
699 we also need a reference profile that represents an unaltered oceanic plate structure. The seaward
700 end points of those projection lines are the possible candidates. The resolution at the seaward end
701 of Line 2 is the best among all segments and at a significant distance away from the trench axis,
702 thus we choose the seaward end of Line 2 to be a reference profile giving the velocity structure
703 of the unaltered incoming plate in the region (Figure 8a). By comparing the shear velocity
704 profiles, we observe that the magnitude of velocity reduction and thus incoming plate hydration
705 is stronger in the Shumagin segment than that in the Semidi segment, consistent with the active
706 source results from Shillington et al (2015). Although the reference velocity profile also shows a
707 small velocity reduction (~0.1 km s^{-1}) atop the mantle, tests in which a series of synthetic
708 dispersion curves were inverted using the same parameterization suggest that the magnitude of
709 such a small velocity reduction was not well constrained by the dispersion data. Besides, we note
710 that the active source profile in this region also shows a significant increase in P-wave velocity
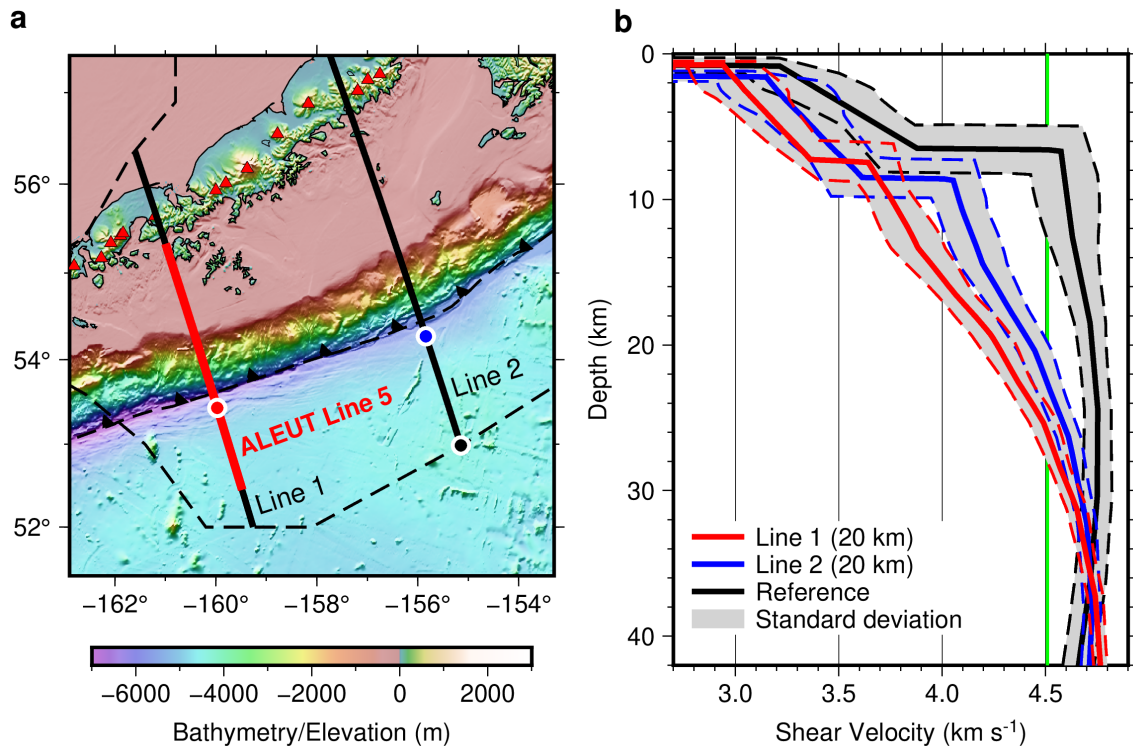711 with depth beneath the moho farther from the trench, consistent with the reference profile.

712

714 **Figure 8**. Velocity profiles on the incoming plate show the upper mantle hydration of the
715 Shumagin segment and the Semidi segment. **(a)** The locations of velocity profiles on cross

716   sections. The red circle on Line 1 and blue circle on Line 2 are chosen 20 km seaward away from
717   the trench axis so that they represent the hydration status at the trench and minimize the spatial
718   smoothing of surface waves. The black circle at the seaward end of Line 2 gives the location of
719   the velocity profile representing the unaltered oceanic plate structure. ALEUT Line 5, shown as
720   the red line, is part of Line 1 (Shillington et al., 2022). **(b)** The 1-D shear velocity profiles of the
721   reference, Line 1 near the trench, and Line 2 near the trench. Here the profile near the trench is
722   chosen at 20 km seaward from the trench axis. The uncertainty contours of each are shown as
723   gray zones. The experimental velocity value of unaltered upper mantle peridotite, 4.51 km s^{-1}, is
724   marked as a green line. The depth is relative to the seafloor.

725

726   Assuming the velocity reduction atop the mantle is purely due to serpentinization, we
727   could use the shear velocity reduction to constrain the hydration. The experimental relationship
728   between shear velocity V_S and serpentine volume fraction (Φ) at 600 MPa is $V_S = 4.51 - 2.19\Phi$
729   for lizardite and chrysotile, and $V_S = 4.51 - 0.84\Phi$ for antigorite (Ji et al., 2013). Experimental
730   work suggests that serpentinization of mantle peridotite forms mostly lizardite at temperatures
731   below 500°C (e.g., Nakatani & Nakamura, 2016), as expected for the uppermost mantle with
732   ages around 50 Ma (Stein & Stein, 1992; McKenzie et al., 2005). The assumption of lizardite
733   mineralogy also results in a conservative estimate of the serpentinization percentage and water
734   content of the mantle. Although the reference velocity profile shows uppermost mantle velocities
735   ranging from 4.55 km s^{-1} to 4.7 km s^{-1}, here we use the experimental value of 4.51 km s^{-1} as the
736   reference velocity of unaltered upper mantle peridotite, which provides a further conservative
737   estimate of the degree of serpentinization and facilitates comparison with other studies. In the
738   Shumagin segment, the shear velocity reduction is 0.87 ± 0.12 km s^{-1} immediately below the
739   Moho (Figure 8b). The velocity reduction then becomes smaller with depth until there is no
740   velocity reduction at 18 ± 3 km below the Moho. The corresponding hydration is roughly
741   equivalent to a 40 ± 6 vol% serpentinization at the top of the mantle, reducing to no
742   serpentinization at 18 ± 3 km below the Moho.

743   Similar calculations can be made for the Semidi segment. Using 4.51 km s^{-1} as the
744   reference value, a 0.46 ± 0.13 km s^{-1} shear velocity reduction is observed right below the Moho,
745   decreasing to no velocity reduction at 14 ± 4 km below the Moho. This gives an estimate of $21 \pm$
746   6 vol% serpentinization at the top of the mantle, decreasing to zero at 14 ± 4 km below the
747   Moho.

748   The maximum degree of serpentinization, as well as the total thickness of the
749   serpentinized layer, is larger in the Shumagin segment compared to that in the Semidi segment,
750   consistent with previous active source results (Shillington et al., 2015). Using the shear velocity
751   reduction at the uppermost mantle, we find that the serpentinization in the Shumagin segment is
752   approximately two times greater than that in the Semidi segment. Carried by the hydrous
753   minerals, more water is expected to input into the deep Earth through the Shumagin segment in
754   the Alaska subduction zone.

755   The distribution of mantle velocity reduction is similar to the distribution of seismicity
756   located by AACSE ocean bottom seismographs (Matulka & Wiens, 2022) as well as mapped
757   fault scarps in seafloor bathymetry (Clarke, 2022) and seismic reflection images (Shillington et
758   al., 2015), consistent with the idea that velocity reduction is caused by hydration from plate-
759   bending faults penetrating into the upper mantle. The Shumagin section shows numerous plate

760   bending faults and has a high seismicity rate, compared to the near-absence of seafloor faults and

761   a lower seismicity rate in the Semedi segment. The depth extent of inferred serpentinization

762   along the Shumagin segment coincides with the depth range of normal faulting earthquakes

763   along plate bending faults (Matulka & Wiens, 2022). The maximum incoming plate seismicity

764   rate occurs 5-10 km below the Moho, and earthquakes are largely limited to depths less than 15-

765   20 km below the Moho, coinciding with the lower limit of serpentinization from this study. The

766   depth range of seismicity in the Semidi segment is similar, but with a much lower seismicity rate.

767   It is worthwhile to compare the Alaska Trench results with the central Mariana Trench

768   (Cai et al., 2018) and the southern Mariana Trench (Zhu et al., 2021). Since the studies use

769   similar techniques, we can directly compare the V_S profiles. The near-trench regions of the

770   central Mariana Trench show uppermost mantle V_S reduced to ~3.5 km s^{-1}, lower than the ~3.65

771   km s^{-1} observed in the Shumagin segment. In addition, the lowered seismic velocities in Mariana

772   extend to about 24 km below the Moho, compared to only 18 km below the Moho in the

773   Shumagin segment. Similar, but less well-constrained velocities and depths were found by Zhu

774   et al. (2021) in the southern Mariana Trench. Cai et al. (2018) interpreted the extremely low

775   incoming plate mantle velocities at the trench as partly due to pore water in the bending faults,

776   and used a velocity of 4.1 km s^{-1} found beneath the forearc after pore water would have been

777   expelled for calculating the degree of serpentinization. The lower velocities and greater depth

778   extent of the mantle velocity reduction suggest a larger percent and extent of mantle

779   serpentinization for Mariana than in the Shumagin or Semidi segments of the Alaska Subduction
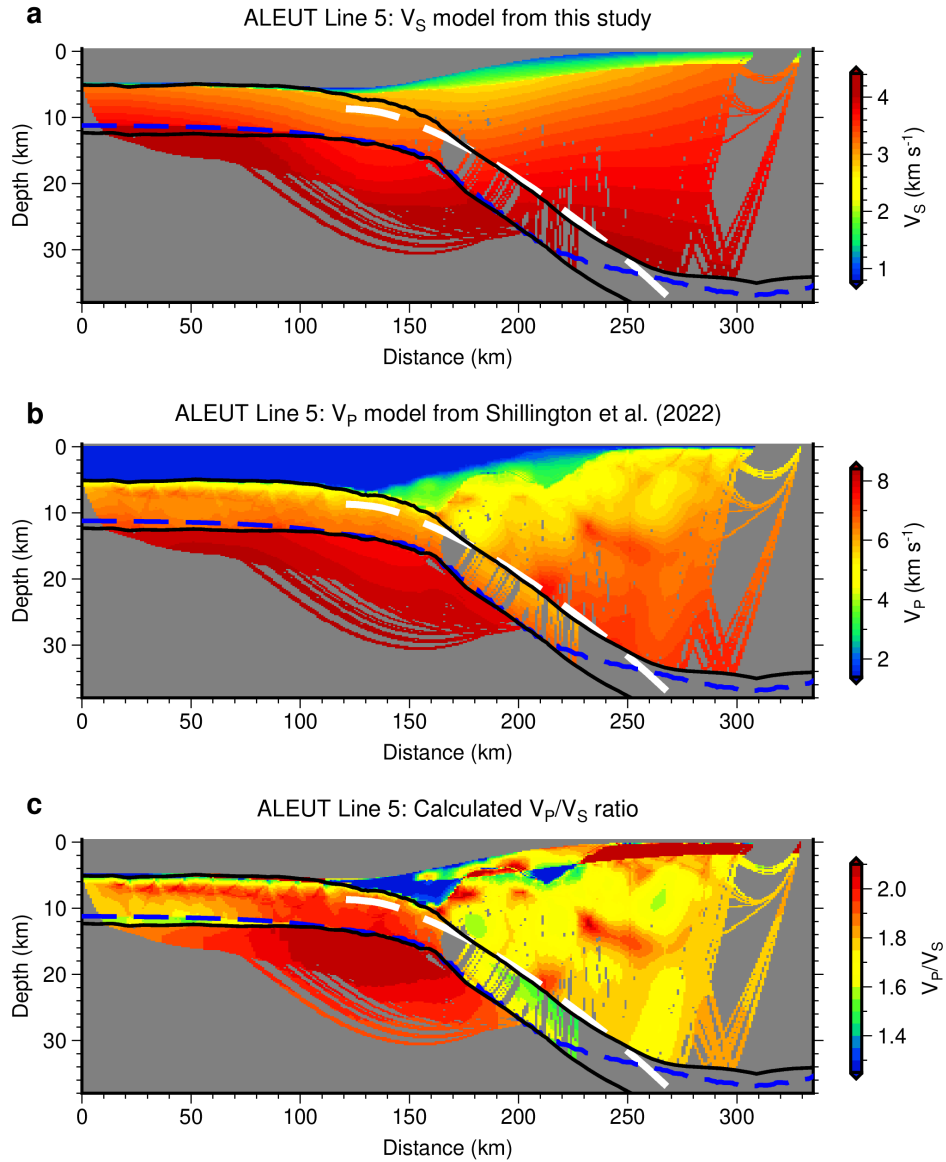
780   Zone.

781

Figure 9. Comparison of the V_S model from this study, the V_P model from Shillington et al. (2022), and the calculated V_P/V_S ratio using two models. The white dashed line shows the depth of slab interface in Slab2.0 model (Hayes et al., 2018). The two solid black lines show boundaries of the V_P model that are constrained by reflections (Shillington et al., 2022), which mark either the ocean bottom, the interface between subducting plate and overriding plate, Moho depth of the overriding plate, or Moho depth of the subducting plate. The dashed blue line shows the Moho depth of the V_S model constrained by this study. **(a)** The shear velocity (V_S) model from this study, which is just a cross-section of the 3-D shear velocity model along the ALEUT Line 5. **(b)** The P-wave velocity (V_P) model from Shillington et al. (2022), which is a 2-D model of the ALEUT Line 5 determined by joint refraction and reflection 2-D tomographic inversion. **(c)** The calculated V_P/V_S ratio using two models along ALEUT Line 5. The colorbar is limited to show the 5- to 95-percentile range of all V_P/V_S values.

796   5.4   Comparison with previous active source results

797   The incoming plate hydration has been previously examined using active-source data
798   (Shillington et al., 2015). In the Shumagin segment, the P-wave velocity of the upper mantle is
799   reduced from 8.2 km s^{-1} to 7.5 km s^{-1}. In the Semidi segment, the P-wave velocities range
800   between 8.0 km s^{-1} to 7.7 km s^{-1}, but do not show a systematic trenchward decrease; these
801   variations may result from heterogeneity in intermediate spreading crust (Shillington et al.,
802   2015). The experimental relationship between V_P and serpentine volume fraction (Φ) at 600 MPa
803   is $V_P = 8.10 - 3.00\Phi$ for lizardite and chrysotile (Ji et al., 2013). For the Shumagin segment, the
804   lowest Vs of 3.64 km s^{-1} is equivalent to ~40 vol% serpentinization, whereas the lowest V_P = 7.5
805   km s^{-1} is equivalent to ~20 vol% serpentinization. Clearly, the serpentinization immediately
806   beneath the Moho estimated from shear velocity reduction tends to be higher than estimates from
807   P-wave velocities.

808   To investigate the differences in hydration estimated from V_P and V_S, we compare the
809   shear velocity model with the active-source P-wave model along the ALEUT Line 5 (Shillington
810   et al., 2022) (Figure 9). The V_P and V_S structures along the same projection line show similar
811   features, though the active source P-wave model exhibits more details and the shear velocity
812   model shows the smoothing effect of surface waves (Figure 9a; Figure 9b). The V_P/V_S ratio
813   (Figure 9c) calculated from the two models shows some small features with extreme values due
814   to the higher resolution and different settings of the slab in the active source P-wave model, but
815   are in general consistent with expected ratios for oceanic and forearc crust. For example, most of
816   the forearc crust has V_P/V_S ratio between 1.65 and 1.85, which is typical for the continental crust
817   (N. I. Christensen, 1996).

818   The crust of the incoming plate shows a distinct region of high V_P/V_S ratio in the plate
819   bending region near the trench. Previous active source studies show large V_S reductions and
820   V_P/V_S ratio increases in the crust of plate-bending regions of various subduction zones (Fujie et
821   al., 2013; Fujie et al., 2018; Grevemeyer et al., 2018). This is generally interpreted as due to the
822   hydration of crustal rocks as well as the additional effect of water in joints and cracks. The high
823   V_P/V_S ratio of the crust of the incoming plate is generally greater than 1.9 for both Kuril Trench
824   and Japan Trench (Fujie et al., 2018), also quite similar to what we observe here (Figure 9c).

825   The incoming plate mantle shows an extremely high V_P/V_S ratio of greater than 2.05 near
826   the trench axis. The experimental relationship between V_P/V_S ratio and serpentine volume
827   fraction (Φ) at 600 MPa is V_P/V_S = 1.77 + 0.38Φ for lizardite and chrysotile, and V_P/V_S = 1.77 +
828   0.04Φ for antigorite (Ji et al., 2013). Using the V_P/V_S = 1.77 + 0.38Φ relationship and V_P/V_S =
829   2.05, we can estimate the serpentinization from V_P/V_S for the uppermost mantle in the Shumagin
830   segment as 73 vol%. This value, of course, is unrealistic but suggests that the serpentinization
831   implied by the V_S reduction, V_P reduction, and V_P/V_S increase are inconsistent.

832   The discrepancy between estimates of serpentinization from V_P, V_S, and the V_P/V_S ratio
833   may result from the effect of water in joints and cracks. Korenaga et al. (2017) showed that
834   modest porosity in crack-like pore spaces with large aspect ratios lowers V_S more significantly
835   than V_P and increases the V_P/V_S ratio. The effect of pore water on the subducting mantle is less
836   well constrained, since most active source surveys are unable to constrain mantle V_S. Cai et al.
837   (2018) attributed part of the large V_S reduction in the Mariana outer-rise mantle to water in
838   cracks and joints. Mark et al. (2023) found evidence from seismic anisotropy for water in crack-
839   like pores in the upper 1 km of the Mariana outer rise mantle using active-source data. If the

840   water in crack-like porosity exists in the mantle, the percent serpentinization determined by V_S
841   values and the V_P/V_S ratios will be overestimated.

842   In the following discussion, we assume that the percent serpentinization of the mantle
843   immediately below the Moho is better estimated by the V_P reduction determined by active source
844   data (Shillington et al., 2015), since the water porosity has a more limited influence on V_P.
845   However, the maximum depth of serpentinization is determined by this study due to the limited
846   depth penetration of the active source results. This discussion assumes that percent
847   serpentinization can be estimated using formulas for bulk serpentinization, as has traditionally
848   been done in previous studies (e.g., Grevemeyer et al., 2018). The actual situation may be more
849   complex, as the serpentinization may be localized in narrow regions surrounding discrete faults
850   (Hatakeyama et al., 2017). In this case, there will be frequency-dependent wave propagation
851   through the mantle at the frequencies used in active source studies (Miller & Lizarralde, 2016;
852   Miller et al., 2021; Mark et al., 2023). Estimates of serpentinization taking this effect into
853   account generally result in smaller percentages of serpentinization, but require analysis of
854   azimuthal anisotropy, which is not available in this case. Therefore we will use the
855   serpentinization estimates based on bulk serpentinization given by Shillington et al. (2015).

856   5.5 Quantitative estimates of subducted water

857   The amount of bound water carried into the Alaska subduction zone by the subducting
858   mantle can be assessed, given estimates of the percentage serpentinization as a function of depth
859   on the incoming plate, since both lizardite and antigorite contain 13% water by weight. The
860   water content of the mantle by weight is calculated from

861   $$w_h = w_s \ \alpha_s \ \rho_s / \rho_m \tag{1}$$

862   where w_s is the weight fraction of water in serpentine, α_s is the volume fraction of serpentine in
863   the mantle determined from seismic measurements, and ρ_s and ρ_m are the densities of serpentine
864   and the mantle, respectively (Carlson & Miller, 2003). Here we assume that serpentinization is
865   maximum at the Moho, where the percent serpentinization is determined from the V_P velocity
866   reduction, and decreases linearly to the maximum depth of serpentinization determined from this
867   study. We do not include any liquid water in pore spaces, since this water will be eliminated with
868   increasing pressure (David et al., 1994) and will not be subducted to significant depths. We also
869   do not explicitly include possible hydrous minerals other than serpentine, such as chlorite and
870   brucite, but note that these other hydrous minerals will also lower the seismic velocity in a
871   similar way to serpentine. Experimental evidence indicates that the dominant hydrous mineral in
872   the incoming plate mantle is likely to be lizardite serpentine (Okamoto et al., 2011).

873   For the Shumagin segment, the V_P reduction from Shillington et al (2015) gives 20%
874   serpentinization at the Moho, decreasing to zero at 18 km below the Moho. The total water
875   content of the hydrated mantle at the Shumagin segment is then equivalent to an 18 km thick,
876   partially serpentinized (10 vol% serpentine, thus 1.0 wt% water) slab mantle layer. Applying the
877   convergence rate of 66 mm yr^{-1} (DeMets et al., 2010), the amount of mantle water input into the
878   Shumagin segment is 37 Tg Myr^{-1} m^{-1}.

879   A similar calculation for the Semedi segment is more uncertain because the evidence of
880   V_P reduction from hydration is less clear in the active-source data. V_P is apparently reduced to
881   7.7 km s^{-1}, but it is unclear whether this is due to hydration or to variability associated with
882   intermediate spreading crust. The V_S reduction observed in this study suggests the reduction is

883 likely due to hydration, in which case we can calculate a serpentinization percentage of 13%
884 from the V_P reduction using the relationships in Ji et al. (2013). Assuming that the
885 serpentinization decreases linearly from 13% at the Moho to zero at a depth of 14 km below the
886 Moho, this is equivalent to a 14 km thick, partially serpentinized (6.5 vol% serpentine, thus 0.6
887 wt% water) hydrated mantle layer. With the convergence rate of 63 mm yr^{-1} (DeMets et al.,
888 2010), this provides an estimate of 17 Tg Myr^{-1} m^{-1} for the flux of mantle water into the Semidi
889 segment. This indicates that the subducting mantle carries more than twice as much water into
890 the Shumagin segment compared to the Semidi segment.

891   These estimates necessarily involve a number of assumptions and are thus only very
892 approximate, but are improvements on previous estimates that made ad-hoc assumptions about
893 the hydration of the subducting mantle (e.g., van Keken et al., 2011), which had no constraint on
894 the depth extent of the serpentinized layer. The largest uncertainty in these estimates is
895 associated with the volume percent of serpentinization, due to the uncertainty of interpreting the
896 discrepant estimates from V_P, V_S, and V_P/V_S, as well as the possible effects of liquid water in
897 crack-like porosity (Korenaga et al., 2017) and anisotropy (Miller & Lizarralde, 2016; Mark et
898 al., 2023). All of the assumptions made in our estimations are conservative and thus result in
899 minimum estimate of subducting water in each segment.

900   These new estimates of subducted mantle water can be combined with previous estimates
901 of water subducted in the crust and sediments to estimate the total water flux. van Keken et al.
902 (2011) did not divide the segments, but estimated that 18 Tg Myr^{-1} m^{-1} subducts in the crust and
903 sediments into the Alaska subduction zone offshore the Alaska Peninsula. Adding this to the
904 mantle estimates gives total subducted water estimates of 55 Tg Myr^{-1} m^{-1} for the Shumagin
905 segment and 35 Tg Myr^{-1} m^{-1} for the Semidi segment. Because the degree of mantle hydration
906 was nearly unconstrained, van Keken et al. (2011) calculated three scenarios for mantle
907 hydration. These estimates were 18 Tg Myr^{-1} m^{-1} for no hydration, 26 Tg Myr^{-1} m^{-1} for 2 wt%
908 water in a 2 km thick mantle layer beneath the Moho, and 53 Tg Myr^{-1} m^{-1} for full
909 serpentinization of a 2 km thick layer. The new estimates exceed the intermediate scenario for
910 both the Shumagin and Semidi segments, and the new estimate for Shumagin is almost identical
911 to the full serpentinization scenario of van Keken et al. (2011).

912   The water flux estimates for both Shumagin and Semidi segments are much less than the
913 94 Tg Myr^{-1} m^{-1} estimated for the total water flux at the Mariana Trench (Cai et al., 2018). This
914 difference results partly from the greater inferred percent serpentinization and the greater depth
915 extent of serpentinization for Mariana. The greater depth extent, as indicated by both the velocity
916 structure and the greater depth of plate bending earthquakes for the Mariana incoming plate
917 (Eimer et al., 2020), may result at least in part from the greater age, and thus greater thickness, of
918 the Mariana lithosphere. On one hand, an older plate has a colder thermal condition and the
919 serpentine could be stable to a greater depth. Antigorite is the main stable phase of serpentine at
920 high temperature, up to ~630°C at 1 GPa (Reynard, 2013; Schwartz et al., 2013). From the recent
921 plate cooling model (Richards et al., 2018), the thermal condition limit of 600°C is 25 km below
922 the seafloor for a 50 Ma plate, and 45 km below the seafloor for a 150 Ma plate. On the other
923 hand, the neutral plane is deeper for older lithosphere and produces a mechanism that could
924 cause deeper stable depth (e.g., Sandiford & Craig, 2023). In addition, the overall extensional
925 stress field of the Mariana arc may be a contributing factor; the slab in the Marianas is dipping
926 more steeply than in the Alaska subduction zone (Nishikawa & Ide, 2015; Hayes et al., 2018).

927   Comparisons of the mantle water flux estimates for Shumagin and Semidi segments and
928 the central Mariana subduction zone suggest that hydration of the uppermost mantle at
929 subduction zones is highly variable. Along-strike changes in hydration can have major effects on
930 intermediate depth and shallow thrust zone seismicity (Shillington et al., 2015; Wei et al., 2021;
931 F. Wang et al., submitted).

932

6 Conclusions

934   We determine a 3-D isotropic shear velocity model of the Alaska subduction zone from a
935 Bayesian Monte Carlo inversion of Rayleigh wave dispersion data using OBS and land station
936 data acquired by the AACSE project and other nearby land networks. A joint inversion including
937 P-wave receiver functions is carried out for land seismic stations.

938   The 3-D model shows major along-strike changes in structure. The forearc structure,
939 including Kodiak Island, appears to have a relatively thick crust (35-42 km) and reduced lower
940 crustal velocities (~3.5 km s^{-1}) from the Kodiak segment to the eastern edge of the Shumagin
941 segment. The eastern portion with distinctive thickened crust is just inboard of the slow lower
942 crustal material extended from the Chugach Terrane. The crustal thickness becomes variable
943 westward of the Shumagin Islands, suggesting that Shumagin Islands may represent a major
944 change in forearc morphology. The continuous low-velocity anomalies observed in the mantle
945 wedge likely represent the hydrous partial melting and melt transport above the slab. The low
946 mantle velocities that extend seaward of the volcanic front into the mantle wedge corner,
947 however, are likely due to serpentinization of the mantle peridotite by water released from the
948 slab immediately below. As for backarc structure, most regions in the northeast are characterized
949 by a relatively typical continental crust. The Bristol Bay Basin, however, shows a significantly
950 reduced crustal thickness and a high-velocity lower crust, indicating a dense mafic composition
951 emplaced during the tectonic extension process that formed the basin.

952   The incoming plate structure shows a low-velocity zone at the top of the subducting
953 oceanic mantle, which results from the serpentinization of mantle peridotite due to water
954 penetrating into the mantle through outer-rise plate-bending faults. Velocity reduction is greater
955 and the thickness of the low-velocity region is larger in the Shumagin segment compared to the
956 Semidi segment. Estimates of serpentinization percentage from V_S reductions and V_P/V_S ratios
957 are larger than that estimated from V_P reduction in Shillington et al. (2015), suggesting that V_S
958 may be strongly affected by liquid water in crack-like pores. Therefore we estimate the
959 serpentinization percentage from the previous V_P results, but use the V_S results to constrain the
960 thickness of the hydrated region. The amount of mantle water input into the strongly hydrated
961 Shumagin segment is about 37 Tg Myr^{-1} m^{-1}, while the amount of mantle water input into the
962 Semidi segment is about 17 Tg Myr^{-1} m^{-1}. Thus the amount of mantle water input into the
963 Shumagin segment is more than twice the mantle water flux into the Semidi segment. However,
964 the amount of water input in both sections is much less than previously estimated for the Mariana
965 incoming plate using similar methods. Water input into subduction zones bound as hydrous
966 minerals in the mantle is highly variable, both between different subduction zones as well as
967 between different segments of the same subduction zone.

968

969

986   **References**

987   Abers, G. A. (1994). Three-dimensional inversion of regional P and S arrival times in the East
988   Aleutians and sources of subduction zone gravity highs. *Journal of Geophysical*
989   *Research: Solid Earth, 99*(B3), 4395-4412. doi:https://doi.org/10.1029/93JB03107
990   Abers, G. A., van Keken, P. E., & Hacker, B. R. (2017). The cold and relatively dry nature of
991   mantle forearcs in subduction zones. *Nature Geoscience, 10*(5), 333-337.
992   doi:10.1038/ngeo2922
993   Acquisto, T. M., Bécel, A., & Canales, J. P. (2022a). *3D traveltime tomography of the Alaska*
994   *subduction zone through inversion of active source data acquired during the Alaska*
995   *Amphibious Community Seismic Experiment (AACSE)*. Paper presented at the AGU Fall
996   Meeting, Chicago, IL. https://ui.adsabs.harvard.edu/abs/2022AGUFM.T25E0169A
997   Acquisto, T. M., Bécel, A., Singh, S. C., & Carton, H. (2022b). Evidence of Strong Upper
998   Oceanic Crustal Hydration Outboard the Alaskan and Sumatran Subduction Zones.
999   *Journal of Geophysical Research: Solid Earth, 127*(10), e2022JB024751.
1000   doi:https://doi.org/10.1029/2022JB024751
1001   Arnulf, A. F., Bassett, D., Harding, A. J., Kodaira, S., Nakanishi, A., & Moore, G. (2022).
1002   Upper-plate controls on subduction zone geometry, hydration and earthquake behaviour.
1003   *Nature Geoscience, 15*(2), 143-148. doi:10.1038/s41561-021-00879-x
1004   Aziz Zanjani, F., & Lin, G. (2022). Double Seismic Zones along the Eastern Aleutian-Alaska
1005   Subduction Zone Revealed by a High-Precision Earthquake Relocation Catalog.
1006   *Seismological Research Letters, 93*(5), 2753-2769. doi:10.1785/0220210348
1007   Bangs, N. L., McIntosh, K. D., Silver, E. A., Kluesner, J. W., & Ranero, C. R. (2015). Fluid
1008   accumulation along the Costa Rica subduction thrust and development of the seismogenic
1009   zone. *Journal of Geophysical Research: Solid Earth, 120*(1), 67-86.
1010   doi:10.1002/2014JB011265

Barcheck, G., Abers, G. A., Adams, A. N., Bécel, A., Collins, J., Gaherty, J. B., . . .
Worthington, L. L. (2020). The Alaska Amphibious Community Seismic Experiment.
Seismological Research Letters. doi:10.1785/0220200189

Barmin, M. P., Ritzwoller, M. H., & Levshin, A. L. (2001). A Fast and Reliable Method for
Surface Wave Tomography. *pure and applied geophysics, 158*(8), 1351-1375.
doi:10.1007/PL00001225

Bassett, D., Arnulf, A., Henrys, S., Barker, D., van Avendonk, H., Bangs, N., . . . Yamamoto, Y.
(2022). Crustal Structure of the Hikurangi Margin From SHIRE Seismic Data and the
Relationship Between Forearc Structure and Shallow Megathrust Slip Behavior.
Geophysical Research Letters, 49(2), e2021GL096960.
doi:https://doi.org/10.1029/2021GL096960

Bécel, A., Shillington, D. J., Delescluse, M., Nedimović, M. R., Abers, Geoffrey A., Saffer, D.
M., . . . Kuehn, H. (2017). Tsunamigenic structures in a creeping section of the Alaska
subduction zone. *Nature Geoscience, 10*(8), 609-613. doi:10.1038/ngeo2990

Bell, S. W., Forsyth, D. W., & Ruan, Y. (2014). Removing Noise from the Vertical Component
Records of Ocean-Bottom Seismometers: Results from Year One of the Cascadia
Initiative. *Bulletin of the Seismological Society of America, 105*(1), 300-313.
doi:10.1785/0120140054

Bensen, G. D., Ritzwoller, M. H., Barmin, M. P., Levshin, A. L., Lin, F., Moschetti, M. P., . . .
Yang, Y. (2007). Processing seismic ambient noise data to obtain reliable broad-band
surface wave dispersion measurements. *Geophysical Journal International, 169*(3), 1239-
1260. doi:10.1111/j.1365-246X.2007.03374.x

Berg, E. M., Lin, F.-C., Allam, A., Schulte-Pelkum, V., Ward, K. M., & Shen, W. (2020). Shear
Velocity Model of Alaska Via Joint Inversion of Rayleigh Wave Ellipticity, Phase
Velocities, and Receiver Functions Across the Alaska Transportable Array. *Journal of
Geophysical Research: Solid Earth, 125*(2), e2019JB018582. doi:10.1029/2019JB018582

Bond, G. C., Lewis, S. D., Taber, J., Steckler, M. S., & Kominz, M. A. (1988). Evidence for
formation of a flexural backarc basin by compression and crustal thickening in the central
Alaska Peninsula. *Geology, 16*(12), 1147-1150. doi:10.1130/0091-
7613(1988)016<1147:EFFOAF>2.3.CO;2

Bradley, D. C., Kusky, T. M., Haeussler, P. J., Goldfarb, R. J., Miller, M. L., Dumoulin, J. A., . .
. Karl, S. M. (2003). Geologic signature of early Tertiary ridge subduction in Alaska. In
V. B. Sisson, S. M. Roeske, & T. L. Pavlis (Eds.), *Geology of a transpressional orogen
developed during ridge-trench interaction along the North Pacific margin* (Vol. 371, pp.
0): Geological Society of America.

Brooks, B. A., Goldberg, D., DeSanto, J., Ericksen, T. L., Webb, S. C., Nooner, S. L., . . . Nevitt,
J. (2023). Rapid shallow megathrust afterslip from the 2021 M8.2 Chignik, Alaska
earthquake revealed by seafloor geodesy. *Sci Adv, 9*(17), eadf9299.
doi:10.1126/sciadv.adf9299

Bruns, T. R., von Huene, R. E., Culotta, R. C., & Lewis, S. D. (1985). *Summary geologic report
for the Shumagin outer continental shelf (OCS) planning area, Alaska* (85-32). Retrieved
from http://pubs.er.usgs.gov/publication/ofr8532

Burstein, J. A., Shillington, D. J., Becel, A., & Nedimovic, M. R. (2022). *Crustal Structure of the
Semidi Segment in the Alaska Subduction Zone Across the 2021 Mw8.2 Chignik
Earthquake Rupture Area Revealed from 2D Wide-Angle Reflection/Refraction Seismic*

Data. Paper presented at the AGU Fall Meeting, Chicago, IL. https://ui.adsabs.harvard.edu/abs/2022AGUFM.T25E0168B

Cai, C., Wiens, D. A., Shen, W., & Eimer, M. (2018). Water input into the Mariana subduction zone estimated from ocean-bottom seismic data. *Nature, 563*(7731), 389-392. doi:10.1038/s41586-018-0655-4

Calvert, A. J., & McGeary, S. E. (2013). Seismic reflection imaging of ultradeep roots beneath the eastern Aleutian island arc. *Geology, 41*(2), 203-206. doi:10.1130/G33683.1

Cameron, C., Prejean, S., Coombs, M., Wallace, K., Power, J., & Roman, D. (2018). Alaska Volcano Observatory Alert and Forecasting Timeliness: 1989–2017. *Frontiers in Earth Science, 6*. doi:10.3389/feart.2018.00086

Carlson, R. L., & Miller, D. J. (2003). Mantle wedge water contents estimated from seismic velocities in partially serpentinized peridotites. *Geophysical Research Letters, 30*(5). doi:10.1029/2002GL016600

Cerpa, N. G., Wada, I., & Wilson, C. R. (2018). Effects of fluid influx, fluid viscosity, and fluid density on fluid migration in the mantle wedge and their implications for hydrous melting. *Geosphere, 15*(1), 1-23. doi:10.1130/GES01660.1

Christensen, D. H., & Ruff, L. J. (1988). SEISMIC COUPLING AND OUTER RISE EARTHQUAKES. *Journal of Geophysical Research: Solid Earth, 93*(B11), 13421-13444. doi:https://doi.org/10.1029/JB093iB11p13421

Christensen, N. I. (1996). Poisson's ratio and crustal seismology. *Journal of Geophysical Research: Solid Earth, 101*(B2), 3139-3156. doi:10.1029/95JB03446

Clarke, J. W. (2022). Controls on bending-related faulting offshore of the Alaska Peninsula. *Masters thesis, Northern Arizona University*. Retrieved from https://openknowledge.nau.edu/id/eprint/5859

Crawford, W. C., & Webb, S. C. (2000). Identifying and Removing Tilt Noise from Low-Frequency (<0.1 Hz) Seafloor Vertical Seismic Data. *Bulletin of the Seismological Society of America, 90*(4), 952-963. doi:10.1785/0119990121

David, C., Wong, T.-F., Zhu, W., & Zhang, J. (1994). Laboratory measurement of compaction-induced permeability change in porous rocks: Implications for the generation and maintenance of pore pressure excess in the crust. *pure and applied geophysics, 143*(1), 425-456. doi:10.1007/BF00874337

Davies, J., Sykes, L., House, L., & Jacob, K. (1981). Shumagin Seismic Gap, Alaska Peninsula: History of great earthquakes, tectonic setting, and evidence for high seismic potential. *Journal of Geophysical Research: Solid Earth, 86*(B5), 3821-3855. doi:https://doi.org/10.1029/JB086iB05p03821

DeMets, C., Gordon, R. G., & Argus, D. F. (2010). Geologically current plate motions. *Geophysical Journal International, 181*(1), 1-80. doi:10.1111/j.1365-246X.2009.04491.x

Drooff, C., & Freymueller, J. T. (2021). New Constraints on Slip Deficit on the Aleutian Megathrust and Inflation at Mt. Veniaminof, Alaska From Repeat GPS Measurements. *Geophysical Research Letters, 48*(4), e2020GL091787. doi:https://doi.org/10.1029/2020GL091787

Eberhart-Phillips, D., Christensen, D. H., Brocher, T. M., Hansen, R., Ruppert, N. A., Haeussler, P. J., & Abers, G. A. (2006). Imaging the transition from Aleutian subduction to Yakutat collision in central Alaska, with local earthquakes and active source data. *Journal of Geophysical Research: Solid Earth, 111*(B11). doi:https://doi.org/10.1029/2005JB004240

Eddy, C. L., & Ekström, G. (2014). Local amplification of Rayleigh waves in the continental United States observed on the USArray. *Earth and Planetary Science Letters, 402*, 50-57. doi:https://doi.org/10.1016/j.epsl.2014.01.013

Eimer, M., Wiens, D. A., Cai, C., Lizarralde, D., & Jasperson, H. (2020). Seismicity of the Incoming Plate and Forearc Near the Mariana Trench Recorded by Ocean Bottom Seismographs. *Geochemistry, Geophysics, Geosystems, 21*(4), e2020GC008953. doi:https://doi.org/10.1029/2020GC008953

Feng, L. (2021). Amphibious Shear Wave Structure Beneath the Alaska-Aleutian Subduction Zone From Ambient Noise Tomography. *Geochemistry, Geophysics, Geosystems, 22*(5), e2020GC009438. doi:https://doi.org/10.1029/2020GC009438

Feng, L., Liu, C., & Ritzwoller, M. H. (2020). Azimuthal Anisotropy of the Crust and Uppermost Mantle Beneath Alaska. *Journal of Geophysical Research: Solid Earth, 125*(12), e2020JB020076. doi:https://doi.org/10.1029/2020JB020076

Feng, L., & Ritzwoller, M. H. (2019). A 3-D Shear Velocity Model of the Crust and Uppermost Mantle Beneath Alaska Including Apparent Radial Anisotropy. *Journal of Geophysical Research: Solid Earth, 124*(10), 10468-10497. doi:https://doi.org/10.1029/2019JB018122

Fisher, M. A., & von Huene, R. E. (1982). *Map showing the geologic structure of the continental shelf southeast and southwest of Kodiak Island, Alaska, from 24-fold seismic data* (1457). Retrieved from http://pubs.er.usgs.gov/publication/mf1457

Fujie, G., Kodaira, S., Kaiho, Y., Yamamoto, Y., Takahashi, T., Miura, S., & Yamada, T. (2018). Controlling factor of incoming plate hydration at the north-western Pacific margin. *Nature Communications, 9*(1), 3844. doi:10.1038/s41467-018-06320-z

Fujie, G., Kodaira, S., Yamashita, M., Sato, T., Takahashi, T., & Takahashi, N. (2013). Systematic changes in the incoming plate structure at the Kuril trench. *Geophysical Research Letters, 40*(1), 88-93. doi:https://doi.org/10.1029/2012GL054340

Furukawa, Y. (1993). Magmatic processes under arcs and formation of the volcanic front. *Journal of Geophysical Research: Solid Earth, 98*(B5), 8309-8319. doi:https://doi.org/10.1029/93JB00350

Gama, I., Fischer, K. M., & Hua, J. (2022). Mapping the Lithosphere and Asthenosphere Beneath Alaska With Sp Converted Waves. *Geochemistry, Geophysics, Geosystems, 23*(10), e2022GC010517. doi:https://doi.org/10.1029/2022GC010517

Gou, T., Xia, S., Huang, Z., & Zhao, D. (2022). Structural Heterogeneity of the Alaska-Aleutian Forearc: Implications for Interplate Coupling and Seismogenic Behaviors. *Journal of Geophysical Research: Solid Earth, 127*(11), e2022JB024621. doi:https://doi.org/10.1029/2022JB024621

Gou, T., Zhao, D., Huang, Z., & Wang, L. (2019). Aseismic Deep Slab and Mantle Flow Beneath Alaska: Insight From Anisotropic Tomography. *Journal of Geophysical Research: Solid Earth, 124*(2), 1700-1724. doi:https://doi.org/10.1029/2018JB016639

Gouédard, P., Seher, T., McGuire, J. J., Collins, J. A., & van der Hilst, R. D. (2014). Correction of Ocean-Bottom Seismometer Instrumental Clock Errors Using Ambient Seismic Noise. *Bulletin of the Seismological Society of America, 104*(3), 1276-1288. doi:10.1785/0120130157

Grevemeyer, I., Hayman, N. W., Peirce, C., Schwardt, M., Van Avendonk, H. J. A., Dannowski, A., & Papenberg, C. (2018). Episodic magmatism and serpentinized mantle exhumation at an ultraslow-spreading centre. *Nature Geoscience, 11*(6), 444-448. doi:10.1038/s41561-018-0124-6

Hatakeyama, K., Katayama, I., Hirauchi, K.-i., & Michibayashi, K. (2017). Mantle hydration along outer-rise faults inferred from serpentinite permeability. *Scientific Reports, 7*(1), 13870. doi:10.1038/s41598-017-14309-9

Hayes, G. P., Moore, G. L., Portner, D. E., Hearne, M., Flamme, H., Furtney, M., & Smoczyk, G. M. (2018). Slab2, a comprehensive subduction zone geometry model. *Science*, eaat4723. doi:10.1126/science.aat4723

He, B., Wei, X., Wei, M., Shen, Y., Alvarez, M., & Schwartz, S. Y. (2023). A shallow slow slip event in 2018 in the Semidi segment of the Alaska subduction zone detected by machine learning. *Earth and Planetary Science Letters, 612*, 118154. doi:https://doi.org/10.1016/j.epsl.2023.118154

Hebert, L. B., Antoshechkina, P., Asimow, P., & Gurnis, M. (2009). Emergence of a low-viscosity channel in subduction zones through the coupling of mantle flow and thermodynamics. *Earth and Planetary Science Letters, 278*(3), 243-256. doi:https://doi.org/10.1016/j.epsl.2008.12.013

Heuret, A., Conrad, C. P., Funiciello, F., Lallemand, S., & Sandri, L. (2012). Relation between subduction megathrust earthquakes, trench sediment thickness and upper plate strain. *Geophysical Research Letters, 39*(5). doi:https://doi.org/10.1029/2011GL050712

Horowitz, W. L., Steffy, D. A., Hoose, P. J., & Turner, R. F. (1989). *Geologic report for the Shumagin planning area, western Gulf of Alaska. Final report*. Retrieved from United States: https://www.osti.gov/biblio/6911563

Hyndman, R. D., & Peacock, S. M. (2003). Serpentinization of the forearc mantle. *Earth and Planetary Science Letters, 212*(3), 417-432. doi:https://doi.org/10.1016/S0012-821X(03)00263-2

Ivandic, M., Grevemeyer, I., Berhorst, A., Flueh, E. R., & McIntosh, K. (2008). Impact of bending related faulting on the seismic properties of the incoming oceanic plate offshore of Nicaragua. *Journal of Geophysical Research: Solid Earth, 113*(B5). doi:https://doi.org/10.1029/2007JB005291

Janiszewski, H. A., Abers, G. A., Shillington, D. J., & Calkins, J. A. (2013). Crustal structure along the Aleutian island arc: New insights from receiver functions constrained by active-source data. *Geochemistry, Geophysics, Geosystems, 14*(8), 2977-2992. doi:https://doi.org/10.1002/ggge.20211

Janiszewski, H. A., Gaherty, J. B., Abers, G. A., Gao, H., & Eilon, Z. C. (2019). Amphibious surface-wave phase-velocity measurements of the Cascadia subduction zone. *Geophysical Journal International, 217*(3), 1929-1948. doi:10.1093/gji/ggz051

Ji, S., Li, A., Wang, Q., Long, C., Wang, H., Marcotte, D., & Salisbury, M. (2013). Seismic velocities, anisotropy, and shear-wave splitting of antigorite serpentinites and tectonic implications for subduction zones. *Journal of Geophysical Research: Solid Earth, 118*(3), 1015-1037. doi:https://doi.org/10.1002/jgrb.50110

Jiang, C., Schmandt, B., Ward, K. M., Lin, F.-C., & Worthington, L. L. (2018). Upper Mantle Seismic Structure of Alaska From Rayleigh and S Wave Tomography. *Geophysical Research Letters, 45*(19), 10,350-310,359. doi:https://doi.org/10.1029/2018GL079406

Jiang, Y., González, P. J., & Bürgmann, R. (2022). Subduction earthquakes controlled by incoming plate geometry: The 2020 M > 7.5 Shumagin, Alaska, earthquake doublet. *Earth and Planetary Science Letters, 584*, 117447. doi:https://doi.org/10.1016/j.epsl.2022.117447

1193   Jin, G., & Gaherty, J. B. (2015). Surface wave phase-velocity tomography based on multichannel
1194   cross-correlation. *Geophysical Journal International, 201*(3), 1383-1398.
1195   doi:10.1093/gji/ggv079

1196   Kahrizi, A., Delescluse, M., Chamot-Rooke, N., Pubellier, M., Bécel, A., Shillington, D., . . .
1197   Bulois, C. (2024). Extensional forearc structures at the transition from Alaska to Aleutian
1198   Subduction Zone: slip partitioning, terranes and large earthquakes. *Comptes Rendus.*
1199   *Géoscience*. doi:10.5802/crgeos.225

1200   Korenaga, J. (2017). On the extent of mantle hydration caused by plate bending. *Earth and*
1201   *Planetary Science Letters, 457*, 1-9. doi:https://doi.org/10.1016/j.epsl.2016.10.011

1202   Korenaga, J., Planavsky, N. J., & Evans, D. A. D. (2017). Global water cycle and the coevolution
1203   of the Earth's interior and surface environment. *Philosophical Transactions of the Royal*
1204   *Society A: Mathematical, Physical and Engineering Sciences, 375*(2094), 20150393.
1205   doi:10.1098/rsta.2015.0393

1206   Kuehn, H. (2019). Along-trench segmentation and down-dip limit of the seismogenic zone at the
1207   eastern Alaska-Aleutian subduction zone.

1208   Kustowski, B., Ekström, G., & Dziewoński, A. M. (2008). Anisotropic shear-wave velocity
1209   structure of the Earth's mantle: A global model. *Journal of Geophysical Research: Solid*
1210   *Earth, 113*(B6). doi:https://doi.org/10.1029/2007JB005169

1211   Li, J., Shillington, D. J., Bécel, A., Nedimović, M. R., Webb, S. C., Saffer, D. M., . . . Kuehn, H.
1212   (2015). Downdip variations in seismic reflection character: Implications for fault
1213   structure and seismogenic behavior in the Alaska subduction zone. *Journal of*
1214   *Geophysical Research: Solid Earth, 120*(11), 7883-7904.
1215   doi:https://doi.org/10.1002/2015JB012338

1216   Li, J., Shillington, D. J., Saffer, D. M., Bécel, A., Nedimović, M. R., Kuehn, H., . . . Abers, G. A.
1217   (2018). Connections between subducted sediment, pore-fluid pressure, and earthquake
1218   behavior along the Alaska megathrust. *Geology, 46*(4), 299-302. doi:10.1130/G39557.1

1219   Li, S., & Freymueller, J. T. (2018). Spatial Variation of Slip Behavior Beneath the Alaska
1220   Peninsula Along Alaska-Aleutian Subduction Zone. *Geophysical Research Letters, 45*(8),
1221   3453-3460. doi:https://doi.org/10.1002/2017GL076761

1222   Ligorría, J. P., & Ammon, C. J. (1999). Iterative deconvolution and receiver-function estimation.
1223   *Bulletin of the Seismological Society of America, 89*(5), 1395-1400.

1224   Lin, F.-C., Moschetti, M. P., & Ritzwoller, M. H. (2008). Surface wave tomography of the
1225   western United States from ambient seismic noise: Rayleigh and Love wave phase
1226   velocity maps. *Geophysical Journal International, 173*(1), 281-298. doi:10.1111/j.1365-
1227   246X.2008.03720.x

1228   Lin, F.-C., & Ritzwoller, M. H. (2011). Helmholtz surface wave tomography for isotropic and
1229   azimuthally anisotropic structure. *Geophysical Journal International, 186*(3), 1104-1120.
1230   doi:10.1111/j.1365-246X.2011.05070.x

1231   Lin, F.-C., Ritzwoller, M. H., & Snieder, R. (2009). Eikonal tomography: surface wave
1232   tomography by phase front tracking across a regional broad-band seismic array.
1233   *Geophysical Journal International, 177*(3), 1091-1110. doi:10.1111/j.1365-
1234   246X.2009.04105.x

1235   Lin, F.-C., Tsai, V. C., & Ritzwoller, M. H. (2012). The local amplification of surface waves: A
1236   new observable to constrain elastic velocities, density, and anelastic attenuation. *Journal*
1237   *of Geophysical Research: Solid Earth, 117*(B6).
1238   doi:https://doi.org/10.1029/2012JB009208

1239 Liu, C., Bai, Y., Lay, T., Feng, Y., & Xiong, X. (2023). Megathrust complexity and the up-dip
1240   extent of slip during the 2021 Chignik, Alaska Peninsula earthquake. *Tectonophysics,*
1241   *854*, 229808. doi:https://doi.org/10.1016/j.tecto.2023.229808
1242 Liu, C., Lay, T., & Xiong, X. (2022). The 29 July 2021 MW 8.2 Chignik, Alaska Peninsula
1243   Earthquake Rupture Inferred From Seismic and Geodetic Observations: Re-Rupture of
1244   the Western 2/3 of the 1938 Rupture Zone. *Geophysical Research Letters, 49*(4),
1245   e2021GL096004. doi:https://doi.org/10.1029/2021GL096004
1246 Liu, C., Lay, T., Xiong, X., & Wen, Y. (2020). Rupture of the 2020 MW 7.8 Earthquake in the
1247   Shumagin Gap Inferred From Seismic and Geodetic Observations. *Geophysical Research*
1248   *Letters, 47*(22), e2020GL090806. doi:https://doi.org/10.1029/2020GL090806
1249 Liu, C., Zhang, S., Sheehan, A. F., & Ritzwoller, M. H. (2022). Surface Wave Isotropic and
1250   Azimuthally Anisotropic Dispersion Across Alaska and the Alaska-Aleutian Subduction
1251   Zone. *Journal of Geophysical Research: Solid Earth, 127*(11), e2022JB024885.
1252   doi:https://doi.org/10.1029/2022JB024885
1253 Lonsdale, P. (1988). Paleogene history of the Kula plate: Offshore evidence and onshore
1254   implications. *GSA Bulletin, 100*(5), 733-754. doi:10.1130/0016-
1255   7606(1988)100<0733:PHOTKP>2.3.CO;2
1256 Lynner, C. (2021). Anisotropy-revealed change in hydration along the Alaska subduction zone.
1257   *Geology*. doi:10.1130/G48860.1
1258 Ma, Z., Dalton, C. A., Russell, J. B., Gaherty, J. B., Hirth, G., & Forsyth, D. W. (2020). Shear
1259   attenuation and anelastic mechanisms in the central Pacific upper mantle. *Earth and*
1260   *Planetary Science Letters, 536*, 116148. doi:https://doi.org/10.1016/j.epsl.2020.116148
1261 Manea, V. C., Leeman, W. P., Gerya, T., Manea, M., & Zhu, G. (2014). Subduction of fracture
1262   zones controls mantle melting and geochemical signature above slabs. *Nature*
1263   *Communications, 5*(1), 5095. doi:10.1038/ncomms6095
1264 Mark, H. F., Lizarralde, D., & Wiens, D. A. (2023). Constraints on Bend-Faulting and Mantle
1265   Hydration at the Marianas Trench From Seismic Anisotropy. *Geophysical Research*
1266   *Letters, 50*(10), e2023GL103331. doi:https://doi.org/10.1029/2023GL103331
1267 Marlow, M. S., Cooper, A. K., & Fisher, M. A. (1994). Geology of the eastern Bering Sea
1268   continental shelf. In G. Plafker & H. C. Berg (Eds.), *The Geology of Alaska* (Vol. G-1,
1269   pp. 0). doi:10.1130/DNAG-GNA-G1.271
1270 Martin-Short, R., Allen, R., Bastow, I. D., Porritt, R. W., & Miller, M. S. (2018). Seismic
1271   Imaging of the Alaska Subduction Zone: Implications for Slab Geometry and Volcanism.
1272   *Geochemistry, Geophysics, Geosystems, 19*(11), 4541-4560. doi:10.1029/2018GC007962
1273 Masson, D. G. (1991). Fault patterns at outer trench walls. *Marine Geophysical Researches,*
1274   *13*(3), 209-225. doi:10.1007/BF00369150
1275 Matulka, P., & Wiens, D. (2022). *Heterogeneous Plate-Bending Earthquake Distribution and*
1276   *Focal Mechanisms Along the Alaska Subduction Zone.* Paper presented at the AGU Fall
1277   Meeting, Chicago, IL. https://ui.adsabs.harvard.edu/abs/2022AGUFM.T32C..03M
1278 McKenzie, D., Jackson, J., & Priestley, K. (2005). Thermal structure of oceanic and continental
1279   lithosphere. *Earth and Planetary Science Letters, 233*(3), 337-349.
1280   doi:https://doi.org/10.1016/j.epsl.2005.02.005
1281 Meyer, B., Chulliat, A., & Saltus, R. (2017). Derivation and Error Analysis of the Earth
1282   Magnetic Anomaly Grid at 2 arc min Resolution Version 3 (EMAG2v3). *Geochemistry,*
1283   *Geophysics, Geosystems, 18*(12), 4522-4537. doi:https://doi.org/10.1002/2017GC007280

Miller, N. C., & Lizarralde, D. (2016). Finite-frequency wave propagation through outer rise fault zones and seismic measurements of upper mantle hydration. *Geophysical Research Letters, 43*(15), 7982-7990. doi:10.1002/2016GL070083

Miller, N. C., Lizarralde, D., Collins, J. A., Holbrook, W. S., & Van Avendonk, H. J. A. (2021). Limited Mantle Hydration by Bending Faults at the Middle America Trench. *Journal of Geophysical Research: Solid Earth, 126*(1), e2020JB020982. doi:https://doi.org/10.1029/2020JB020982

Moore, J. C., Diebold, J., Fisher, M. A., Sample, J., Brocher, T., Talwani, M., . . . Sawyer, D. (1991). EDGE deep seismic reflection transect of the eastern Aleutian arc-trench layered lower crust reveals underplating and continental growth. *Geology, 19*(5), 420-424. doi:10.1130/0091-7613(1991)019<0420:EDSRTO>2.3.CO;2

Nakatani, T., & Nakamura, M. (2016). Experimental constraints on the serpentinization rate of fore-arc peridotites: Implications for the upwelling condition of the slab-derived fluid. *Geochemistry, Geophysics, Geosystems, 17*(8), 3393-3419. doi:https://doi.org/10.1002/2016GC006295

Naliboff, J. B., Billen, M. I., Gerya, T., & Saunders, J. (2013). Dynamics of outer-rise faulting in oceanic-continental subduction systems. *Geochemistry, Geophysics, Geosystems, 14*(7), 2310-2327. doi:https://doi.org/10.1002/ggge.20155

Nishikawa, T., & Ide, S. (2015). Background seismicity rate at subduction zones linked to slab-bending-related hydration. *Geophysical Research Letters, 42*(17), 7081-7089. doi:https://doi.org/10.1002/2015GL064578

Okamoto, A., Ogasawara, Y., Ogawa, Y., & Tsuchiya, N. (2011). Progress of hydration reactions in olivine–H_2O and orthopyroxenite–H_2O systems at 250°C and vapor-saturated pressure. *Chemical Geology, 289*(3), 245-255. doi:https://doi.org/10.1016/j.chemgeo.2011.08.007

Qi, C., Zhao, D., Chen, Y., & Ruppert, N. A. (2007). New insight into the crust and upper mantle structure under Alaska. *Polar Science, 1*(2), 85-100. doi:https://doi.org/10.1016/j.polar.2007.07.001

Ranero, C. R., Phipps Morgan, J., McIntosh, K., & Reichert, C. (2003). Bending-related faulting and mantle serpentinization at the Middle America trench. *Nature, 425*(6956), 367-373. doi:10.1038/nature01961

Rees Jones, D. W., Katz, R. F., Tian, M., & Rudge, J. F. (2018). Thermal impact of magmatism in subduction zones. *Earth and Planetary Science Letters, 481*, 73-79. doi:https://doi.org/10.1016/j.epsl.2017.10.015

Reynard, B. (2013). Serpentine in active subduction zones. *Lithos, 178*, 171-185. doi:https://doi.org/10.1016/j.lithos.2012.10.012

Richards, F. D., Hoggard, M. J., Cowton, L. R., & White, N. J. (2018). Reassessing the Thermal Structure of Oceanic Lithosphere With Revised Global Inventories of Basement Depths and Heat Flow Measurements. *Journal of Geophysical Research: Solid Earth, 123*(10), 9136-9161. doi:https://doi.org/10.1029/2018JB015998

Ruff, L. J. (1989). Do trench sediments affect great earthquake occurrence in subduction zones? *pure and applied geophysics, 129*(1), 263-282. doi:10.1007/BF00874629

Ruppert, N. A., Barcheck, G., & Abers, G. A. (2022). Enhanced Regional Earthquake Catalog with Alaska Amphibious Community Seismic Experiment Data. *Seismological Research Letters, 94*(1), 522-530. doi:10.1785/0220220226

1329   Russell, J. B., & Dalton, C. A. (2022). Rayleigh Wave Attenuation and Amplification Measured
1330   at Ocean-Bottom Seismometer Arrays Using Helmholtz Tomography. *Journal of*
1331   *Geophysical Research: Solid Earth, 127*(10), e2022JB025174.
1332   doi:https://doi.org/10.1029/2022JB025174

1333   Sadofsky, S. J., Portnyagin, M., Hoernle, K., & van den Bogaard, P. (2008). Subduction cycling
1334   of volatiles and trace elements through the Central American volcanic arc: evidence from
1335   melt inclusions. *Contributions to Mineralogy and Petrology, 155*(4), 433-456.
1336   doi:10.1007/s00410-007-0251-3

1337   Sallarès, V., & Ranero, C. R. (2019). Upper-plate rigidity determines depth-varying rupture
1338   behaviour of megathrust earthquakes. *Nature, 576*(7785), 96-101. doi:10.1038/s41586-
1339   019-1784-0

1340   Sample, J. C., & Moore, J. C. (1987). Structural style and kinematics of an underplated slate belt,
1341   Kodiak and adjacent islands, Alaska. *GSA Bulletin, 99*(1), 7-20. doi:10.1130/0016-
1342   7606(1987)99<7:SSAKOA>2.0.CO;2

1343   Sandiford, D., & Craig, T. J. (2023). Plate bending earthquakes and the strength distribution of
1344   the lithosphere. *Geophysical Journal International, 235*(1), 488-508.
1345   doi:10.1093/gji/ggad230

1346   Scholl, D. W., Kirby, S. H., von Huene, R., Ryan, H., Wells, R. E., & Geist, E. L. (2015). Great
1347   ($\geq$Mw8.0) megathrust earthquakes and the subduction of excess sediment and
1348   bathymetrically smooth seafloor. *Geosphere, 11*(2), 236-265. doi:10.1130/GES01079.1

1349   Schwartz, S., Guillot, S., Reynard, B., Lafay, R., Debret, B., Nicollet, C., . . . Auzende, A. L.
1350   (2013). Pressure–temperature estimates of the lizardite/antigorite transition in high
1351   pressure serpentinites. *Lithos, 178*, 197-210.
1352   doi:https://doi.org/10.1016/j.lithos.2012.11.023

1353   Shellenbaum, D. P., Gregersen, L. S., & Delaney, P. R. (2010). Top Mesozoic unconformity
1354   depth map of the Cook Inlet Basin, Alaska, Alaska Div. *Geol. Geophys. Surv. Report of*
1355   *Investigation, 2*(1).

1356   Shen, W., & Ritzwoller, M. H. (2016). Crustal and uppermost mantle structure beneath the
1357   United States. *Journal of Geophysical Research: Solid Earth, 121*(6), 4306-4342.
1358   doi:https://doi.org/10.1002/2016JB012887

1359   Shen, W., Ritzwoller, M. H., Kang, D., Kim, Y., Lin, F.-C., Ning, J., . . . Zhou, L. (2016). A
1360   seismic reference model for the crust and uppermost mantle beneath China from surface
1361   wave dispersion. *Geophysical Journal International, 206*(2), 954-979.
1362   doi:10.1093/gji/ggw175

1363   Shen, W., Ritzwoller, M. H., Schulte-Pelkum, V., & Lin, F.-C. (2013). Joint inversion of surface
1364   wave dispersion and receiver functions: a Bayesian Monte-Carlo approach. *Geophysical*
1365   *Journal International, 192*(2), 807-836. doi:10.1093/gji/ggs050

1366   Shen, W., Wiens, D. A., Anandakrishnan, S., Aster, R. C., Gerstoft, P., Bromirski, P. D., . . .
1367   Winberry, J. P. (2018). The Crust and Upper Mantle Structure of Central and West
1368   Antarctica From Bayesian Inversion of Rayleigh Wave and Receiver Functions. *Journal*
1369   *of Geophysical Research: Solid Earth, 123*(9), 7824-7849.
1370   doi:https://doi.org/10.1029/2017JB015346

1371   Shillington, D. J., Bécel, A., & Nedimović, M. R. (2022). Upper Plate Structure and Megathrust
1372   Properties in the Shumagin Gap Near the July 2020 M7.8 Simeonof Event. *Geophysical*
1373   *Research Letters, 49*(2), e2021GL096974. doi:https://doi.org/10.1029/2021GL096974

Shillington, D. J., Bécel, A., Nedimović, M. R., Kuehn, H., Webb, S. C., Abers, G. A., . . . Mattei-Salicrup, G. A. (2015). Link between plate fabric, hydration and subduction zone seismicity in Alaska. *Nature Geoscience, 8*(12), 961-964. doi:10.1038/ngeo2586

Silwal, V., Tape, C., & Lomax, A. (2018). Crustal earthquakes in the Cook Inlet and Susitna region of southern Alaska. *Tectonophysics, 745*, 245-263. doi:https://doi.org/10.1016/j.tecto.2018.08.013

Stehly, L., Campillo, M., & Shapiro, N. M. (2007). Traveltime measurements from noise correlation: stability and detection of instrumental time-shifts. *Geophysical Journal International, 171*(1), 223-230. doi:10.1111/j.1365-246X.2007.03492.x

Stein, C. A., & Stein, S. (1992). A model for the global variation in oceanic depth and heat flow with lithospheric age. *Nature, 359*(6391), 123-129. doi:10.1038/359123a0

Tian, Y., & Ritzwoller, M. H. (2017). Improving ambient noise cross-correlations in the noisy ocean bottom environment of the Juan de Fuca plate. *Geophysical Journal International, 210*(3), 1787-1805. doi:10.1093/gji/ggx281

Tian, Y., & Zhao, D. (2012). Seismic anisotropy and heterogeneity in the Alaska subduction zone. *Geophysical Journal International, 190*(1), 629-649. doi:10.1111/j.1365-246X.2012.05512.x

Van Avendonk, H. J. A., Holbrook, W. S., Lizarralde, D., & Denyer, P. (2011). Structure and serpentinization of the subducting Cocos plate offshore Nicaragua and Costa Rica. *Geochemistry, Geophysics, Geosystems, 12*(6). doi:10.1029/2011GC003592

van Keken, P. E., Hacker, B. R., Syracuse, E. M., & Abers, G. A. (2011). Subduction factory: 4. Depth-dependent flux of H2O from subducting slabs worldwide. *Journal of Geophysical Research: Solid Earth, 116*(B1). doi:https://doi.org/10.1029/2010JB007922

von Huene, R., Miller, J. J., & Krabbenhoeft, A. (2019). The Shumagin seismic gap structure and associated tsunami hazards, Alaska convergent margin. *Geosphere, 15*(2), 324-341. doi:10.1130/GES01657.1

von Huene, R., Miller, J. J., & Krabbenhoeft, A. (2021). The Alaska Convergent Margin Backstop Splay Fault Zone, a Potential Large Tsunami Generator Between the Frontal Prism and Continental Framework. *Geochemistry, Geophysics, Geosystems, 22*(1), e2019GC008901. doi:https://doi.org/10.1029/2019GC008901

von Huene, R., Miller, J. J., & Weinrebe, W. (2012). Subducting plate geology in three great earthquake ruptures of the western Alaska margin, Kodiak to Unimak. *Geosphere, 8*(3), 628-644. doi:10.1130/GES00715.1

Walker, K. T., McGeary, S. E., & Klemperer, S. L. (2003). Tectonic Evolution of the Bristol Bay basin, southeast Bering Sea: Constraints from seismic reflection and potential field data. *Tectonics, 22*(5). doi:https://doi.org/10.1029/2002TC001359

Wang, F., Wei, S. S., Drooff, C., Elliott, J., Freymueller, J. T., Ruppert, N., & Zhang, H. (submitted). Fluids controlling along-strike variations in the Alaska megathrust slip. *Nature*.

Wang, Y., & Tape, C. (2014). Seismic velocity structure and anisotropy of the Alaska subduction zone based on surface wave tomography. *Journal of Geophysical Research: Solid Earth, 119*(12), 8845-8865. doi:https://doi.org/10.1002/2014JB011438

Ward, K. M. (2015). Ambient noise tomography across the southern Alaskan Cordillera. *Geophysical Research Letters, 42*(9), 3218-3227. doi:https://doi.org/10.1002/2015GL063613

1419   Ward, K. M., & Lin, F.-C. (2018). Lithospheric Structure Across the Alaskan Cordillera From
1420   the Joint Inversion of Surface Waves and Receiver Functions. *Journal of Geophysical*
1421   *Research: Solid Earth, 123*(10), 8780-8797. doi:https://doi.org/10.1029/2018JB015967
1422   Webb, S. C., & Crawford, W. C. (1999). Long-period seafloor seismology and deformation
1423   under ocean waves. *Bulletin of the Seismological Society of America, 89*(6), 1535-1542.
1424   Wei, S. S., Ruprecht, P., Gable, S. L., Huggins, E. G., Ruppert, N., Gao, L., & Zhang, H. (2021).
1425   Along-strike variations in intermediate-depth seismicity and arc magmatism along the
1426   Alaska Peninsula. *Earth and Planetary Science Letters, 563*, 116878.
1427   doi:https://doi.org/10.1016/j.epsl.2021.116878
1428   Wiens, D. A., Conder, J. A., & Faul, U. H. (2008). The Seismic Structure and Dynamics of the
1429   Mantle Wedge. *Annual Review of Earth and Planetary Sciences, 36*(1), 421-455.
1430   doi:10.1146/annurev.earth.33.092203.122633
1431   Wilson, C. R., Spiegelman, M., van Keken, P. E., & Hacker, B. R. (2014). Fluid flow in
1432   subduction zones: The role of solid rheology and compaction pressure. *Earth and*
1433   *Planetary Science Letters, 401*, 261-274. doi:https://doi.org/10.1016/j.epsl.2014.05.052
1434   Xiao, Z., Freymueller, J. T., Grapenthin, R., Elliott, J. L., Drooff, C., & Fusso, L. (2021). The
1435   deep Shumagin gap filled: Kinematic rupture model and slip budget analysis of the 2020
1436   Mw 7.8 Simeonof earthquake constrained by GNSS, global seismic waveforms, and
1437   floating InSAR. *Earth and Planetary Science Letters, 576*, 117241.
1438   doi:https://doi.org/10.1016/j.epsl.2021.117241
1439   Yang, X., & Gao, H. (2020). Segmentation of the Aleutian-Alaska Subduction Zone Revealed by
1440   Full-Wave Ambient Noise Tomography: Implications for the Along-Strike Variation of
1441   Volcanism. *Journal of Geophysical Research: Solid Earth, 125*(11), e2020JB019677.
1442   doi:https://doi.org/10.1029/2020JB019677
1443   Ye, S., Flueh, E. R., Klaeschen, D., & von Huene, R. (1997). Crustal structure along the EDGE
1444   transect beneath the Kodiak shelf off Alaska derived from OBH seismic refraction data.
1445   *Geophysical Journal International, 130*(2), 283-302. doi:10.1111/j.1365-
1446   246X.1997.tb05648.x
1447   Zhao, D., Wang, Z., Umino, N., & Hasegawa, A. (2007). Tomographic Imaging outside a
1448   Seismic Network: Application to the Northeast Japan Arc. *Bulletin of the Seismological*
1449   *Society of America, 97*(4), 1121-1132. doi:10.1785/0120050256
1450   Zhu, G., Wiens, D. A., Yang, H., Lin, J., Xu, M., & You, Q. (2021). Upper Mantle Hydration
1451   Indicated by Decreased Shear Velocity Near the Southern Mariana Trench From
1452   Rayleigh Wave Tomography. *Geophysical Research Letters, 48*(15), e2021GL093309.
1453   doi:https://doi.org/10.1029/2021GL093309
1454